

# Inferring hemispheric asymmetries of stellar active regions through the information content of astrometric signals

C. Deagan,<sup>1</sup> Benjamin T. Montet,<sup>1</sup> 

<sup>1</sup>School of Physics, University of New South Wales, Sydney, NSW 2052, Australia

Accepted XXX. Received YYY; in original form ZZZ

## ABSTRACT

Photometric light curves suffer from fundamental degeneracies that limit surface information recovery. We demonstrate that astrometry enables access to complementary information through photocentre variations induced by rotating surface features. The forthcoming commissioning of microarcsecond-precision astrometric missions presents an opportunity to improve stellar surface mapping. This paper extends a previous theoretical framework for stellar surface mapping, along three primary directions: (1) we derive analytical selection rules showing that astrometry is sensitive to spherical harmonic modes not detectable via photometry, particularly odd- $\ell$  modes that encode north-south asymmetries; (2) we quantify the information content of combined photometric and astrometric observations, showing that the rank of observable modes grows faster for combined observations than for either technique alone, though the fraction of recoverable modes still decreases asymptotically with increasing spatial resolution; and (3) we reframe astrometric jitter—traditionally treated as noise in exoplanet studies—as a signal encoding stellar surface structure. Given the limited proposed target lists of high-precision astrometric missions, this capability is particularly valuable: understanding host star surfaces is crucial for both removing stellar signals from exoplanet detections and characterising star-planet interactions. We show that while Sun-like stars require sub-microarcsecond precision, evolved stars with angular diameter and larger spots present immediate opportunities with current technology, such as the Gaia mission.

**Key words:** astrometry — stars: activity — stars: imaging — stars: spots

## 1 INTRODUCTION

Stellar surfaces provide directly observable manifestations of the physical processes that operate within the interior of stars. Any photon produced by a star can tell us about its internal mechanisms, whether they originate from flares (Kowalski 2024), star spots or the quiet photosphere (e.g. Berdyugina 2005). Via time series observations of stellar surfaces, we can learn about differential rotation (e.g., Croll et al. 2006; Reinhold et al. 2013), magnetic activity cycles (e.g., Montet et al. 2017; Morris et al. 2018a), large-scale magnetic dynamos (e.g., Berdyugina 2005; Roettenbacher et al. 2016), and space weather around other stars (Zic et al. 2020). For Sun-like stars, magnetically driven phenomena primarily manifest as surface inhomogeneities: dark spots arising from regions of magnetically suppressed convection, bright faculae and networks in the photosphere, and chromospheric plages and prominences. All of these features affect stellar observables as they emerge, decay, and rotate across the stellar surface (Rackham et al. 2023). Not only is this knowledge useful for stellar physics (see references above), but it is important for exoplanet characterisation, where stellar activity is often the dominant source of uncertainty and contamination.

The fundamental challenge in stellar surface mapping stems from stars being far away. Nearly all stars, particularly Sun-like stars, remain spatially unresolved with current technologies. A handful of nearby giant stars can be resolved using interferometry (e.g., Evans

et al. 2024). Spatial unresolvability compresses the complexity of the two-dimensional stellar surfaces into observables such as photometry, spectroscopy, Doppler imaging, Zeeman Doppler imaging (ZDI), interferometry, and astrometry, among others. Many of these techniques are one-dimensional. Each technique probes different aspects of the stellar surface, and each suffers from degeneracies that prevent unique surface reconstruction (Rice 2002; Luger et al. 2021; Dholakia & Pope 2025). These techniques are all useful, but care must be taken to ensure that any inferences regarding the surface of stars is actually constrained by the information provided by the observational techniques, rather than imposed by a prior. For example, the differences in surface reconstruction in Roettenbacher et al. (2017) likely come from a combination of degeneracies between each method, and priors (explicit or otherwise) that have been imposed to deal with said degeneracies.

This inverse problem of reconstructing stellar surfaces from observables such as light curves has been well known for a long time. Russell (1906) demonstrated that there are an infinite number of surface configurations that could produce the same light curve for any convex rotating body. He used the fact that all odd degree spherical harmonics do not appear in the light curve and thus the coefficients to these harmonics could take on any value.

Further complications come from the finite lifetimes of surface features. Sunspot lifetimes scale linearly with their maximum area (Hathaway & Choudhary 2008; Muraközy 2021), with larger Sun spots/spot groups lasting for weeks to months. Spots on Solar-type stars can last up to 350 days (Namekata et al. 2019), and a spot group

\* E-mail: c.deagan@unsw.edu.au

has persisted for 16 years on an M4 dwarf (Vida et al. 2016). While the vast majority of Sun spots are short lived, the size distribution of Sun spots is log-normal, with small spots being much more prevalent than large spots (Baumann & Solanki 2005). Current levels of instrumental precision mean that only the larger star spots will have an impact on observables, as small spots will be dwarfed by noise. Additionally, spot evolution violates the common assumption of static surfaces in mapping algorithms and can mimic differential rotation signatures (Basri 2018).

Multiple complementary techniques have been developed to extract surface information, each with advantages and limitations:

(i) Photometric light curve inversion leverages rotational modulation to reproduce the surface features that created the variations in the light curve. This technique often operates on differential rather than absolute light curves, a distinction that can impact the surface recovery (see discussions regarding this in Basri 2018; Luger et al. 2021). While successful in identifying large-scale spot patterns, light curve inversion suffers from the fundamental degeneracies we described above. Multi-band photometry can help constrain surfaces by exploiting temperature-dependent blackbody emission. Brightness variations occur due to surface temperature inhomogeneities, which can provide spot temperature constraints (e.g., Morris et al. 2018b). Additionally, priors enforcing spot compactness or maximum entropy distribution help regularise solutions. Nevertheless, recovered maps remain non-unique and are potentially biased by prior assumptions.

(ii) Doppler imaging uses distortions in spectral line profiles as features cross the visible disk. This technique typically requires high-resolution spectroscopy for sufficient line resolution and rapid rotation so that rotational broadening dominates the line profile. Angular resolution increases with stellar rotational velocity (Kochukhov 2016). The achievable resolution for Sun-like stars is typically low: a recent study obtained brightness maps with angular resolution of  $\approx 36^\circ$  (Klein et al. 2025). Because the rotational Doppler shift depends on projected velocity, the latitude of surface features can be inferred; however, Doppler imaging is insensitive to the sign of the latitude, leading to a north–south degeneracy for spots mirrored across the equator. The technique suffers from two related limitations: latitude smearing near the stellar equator, where the variation of radial velocity with time depends only weakly on latitude (Rice & Strassmeier 1998), and degraded latitude discrimination at low stellar inclinations, where the projected velocity range is compressed and latitudinal information is generally less well constrained. Recent combinations of Doppler imaging with photometry can partially break these degeneracies (Kővári et al. 2021). Kochukhov (2016) discusses the ill-posed nature of Doppler imaging in detail.

(iii) Zeeman Doppler imaging (ZDI) extends Doppler imaging by exploiting the polarization signatures induced by the Zeeman effect in spectral lines to recover information about the stellar magnetic field. As the Zeeman effect is often small, ZDI tends to be limited to bright, magnetically active, rapidly rotating stars (Walkowicz et al. 2013). ZDI preferentially recovers large scale field structures and misses smaller scale magnetic complexity. This is partly because unresolved spot pairs with opposite polarities cancel each other out (Kochukhov 2016; Morris et al. 2017). As with other inversion methods, ZDI is ill-posed and the recovered topology often depends on the chosen regularisation schema (Carroll et al. 2008).

(iv) Interferometry is the only direct means of resolving stellar disks, providing the only technique capable of distinguishing brightness variations across the stellar surface in both latitude and longitude without requiring rotational modulation. Surface reconstructions do

not require *a priori* information (Roettenbacher et al. 2017). Using long-baseline arrays such as CHARA and VLTI, surface structure such as starspots and convection patterns have been imaged on evolved giants like  $\sigma$  Gem and Betelgeuse (Haubois et al. 2009; Roettenbacher et al. 2017). Like other techniques, interferometry is also ill-posed. Incomplete uv coverage and a lack of phase information mean that intensity interferometry contains analytical degeneracies, as discussed by Dholakia & Pope (2025).

These methods can each provide useful surface reconstructions, particularly when combined (see Dholakia & Pope 2025). In a comparative study, Roettenbacher et al. (2017) examined the consistency of independent reconstructions by applying three different techniques: interferometry, Doppler imaging, and light curve inversion. They created three independent reconstructions of  $\sigma$  Gem (a spotted giant star) across two epochs using contemporaneous observations. The reconstructions showed longitudinally consistent spot features; however, they exhibited strong disagreement in spot latitudes. The disagreement between the surfaces worsened during the epoch where the surface appeared to be more complex. These authors demonstrate the need for caution when interpreting surface reconstructions.

Additional constraints on stellar surface features can arise from chance geometric alignments. Eclipsing binaries and transiting exoplanets provide unique opportunities to break mapping degeneracies, as the occulter disrupts the symmetries that make latitude determination particularly challenging in rotational mapping (Luger et al. 2019). Spot occultation events produce characteristic signatures in transit light curves (and other observables) that enable direct localisation of spots along the transit chord (Morris et al. 2017). While these techniques require fortuitous orbital configurations and are therefore not available for arbitrary stars, when they do occur, they can help provide much tighter constraints on surface reconstruction.

This paper demonstrates that high-precision astrometry, measurements of stellar photocentre positions at microarcsecond levels, provides surface information orthogonal to existing techniques, breaking degeneracies that have limited surface mapping. As surface inhomogeneities rotate across the stellar disk, they shift the intensity-weighted centroid, photocentre, from the geometric centre, producing time-varying astrometric deflections that encode both the amplitude and spatial distribution of brightness variations (Eriksson & Lindegren 2007; Makarov et al. 2009, Deagan et al., submitted.). The astrometric signal possesses three advantages compared to photometry. First, it provides an inherently two-dimensional observable — both  $x$  and  $y$  photocentre positions — with orthogonal components sampling different surface information. Second, astrometry exhibits sensitivity to spherical harmonic modes that lie entirely within the photometric null space, particularly odd- $\ell$  modes encoding north–south asymmetries. Third, the position-weighted nature of the observable means that identical flux deficits at different disk locations produce distinct astrometric signatures, breaking the positional degeneracy that can occur in photometry. Recent technological developments make microarcsecond astrometry increasingly feasible. The Gaia mission has demonstrated 10–100 microarcsecond precision for millions of stars (Vallenari et al. 2023). With the upcoming release of Gaia DR4, activity induced jitter will be able to inform us about the surface of nearby giant stars with large spots. Proposed next-generation missions push toward even higher precision: TOLIMAN aims for sub-microarcsecond measurements of  $\alpha$  Centauri A and B through narrow-angle differential astrometry (Tuthill et al. 2018), while concepts like Theia (The Theia Collaboration et al. 2017), MASS (Nemati et al. 2020), small-JASMINE (Utsunomiya et al.

2014), CHES (Ji et al. 2022), and ARMADA (Gardner et al. 2022) target microarcsecond precision for larger samples. Ground-based efforts using techniques like diffractive pupil technology show promise for achieving comparable precision from Earth (Bendek et al. 2021; Gardner et al. 2022). Importantly, astrometric planet-hunting missions naturally provide stellar surface information as a by-product. The same photocentre measurements designed to detect planetary reflex motion also encode surface structure through activity-induced jitter. Rather than treating this jitter as noise to be minimised, we demonstrate that it represents a valuable signal complementary to photometry. Since astrometric instruments inherently provide simultaneous photometry, the combined dataset enables more surface constraints via the use of two observational techniques with just a single instrument.

This paper extends the theoretical framework developed by Luger et al. (2021), and applied by Dholakia & Pope (2025), for understanding the information content of photometric signals and extends it to astrometric signals. Section 2 develops the mathematical foundation, deriving the observation operators in the spherical-harmonic basis and establishing analytical selection rules that reveal which surface modes are accessible to each technique. In Section 4 we introduce the numerical model that we use to model astrometric observations. In Section 5 we use numerical simulations across arbitrary viewing geometries to quantify the recoverable information and show that combined photometric–astrometric data unlocks substantially more modes than photometry alone, though the fraction of accessible modes still decreases with spatial resolution. Section 6 discusses limitations, practical implications including mission/instrument design considerations, and applications to stellar physics and exoplanet science. We particularly emphasise how understanding activity-induced astrometric jitter is essential for detecting Earth-like planets, as the signals are comparable in magnitude. Section 7 discusses activity-induced photocentre shifts, how microarcsecond astrometry quantifies them, how they should be treated, and how astrometry provides complementary constraints to photometry.

## 2 THEORETICAL BACKGROUND

In this section, we establish the mathematical framework that we use to analyse the information content of stellar surface observables. We extend the analysis of Luger et al. (2021) to include astrometric measurements and demonstrate that astrometry enables access to additional complementary spherical harmonic modes to the modes recoverable via photometry. We adopt the spherical harmonic notation with polar angle  $\theta \in [0, \pi]$  (where  $\theta = 0, \pi$  correspond to the poles), and azimuthal angle  $\varphi \in [0, 2\pi]$ , with the polar axis aligned with the stellar rotation axis.

### 2.1 Spherical Harmonics

Spherical harmonics provide a natural framework for describing stellar surfaces. Assuming stars behave as rotating spheres of uniform radius, neglecting any photospheric height variations and the finite extent of surface structures, then the surface brightness distribution  $I(\theta, \varphi)$  can be uniquely decomposed as:

$$I(\theta, \varphi) = \sum_{\ell=0}^{\infty} \sum_{m=-\ell}^{\ell} a_{\ell}^m Y_{\ell}^m(\theta, \varphi) \quad (1)$$

where  $Y_{\ell}^m(\theta, \varphi)$  are the real spherical harmonics of degree  $\ell$  and order  $m$  (defined explicitly in the appendix — see Eq (A1)), and

the coefficients  $\{a_{\ell}^m\}$  completely specify the surface structure. This expansion is exact for any square-integrable function on the sphere. Spherical harmonics provide a complete, linear, orthonormal basis. From an information theory perspective, each spherical harmonic mode represents an independent degree of freedom in the surface brightness distribution. The total information content of the surface is therefore encoded in the full set of coefficients  $\{a_{\ell}^m\}$ .

The degree  $\ell$  controls the characteristic angular scale of features, with an approximate angular size of  $\approx 180^\circ/\ell$ . Low degree modes represent large scale structures, and higher degree modes represent finer surface structure. The order  $m$  encodes the azimuthal (longitudinal) structure.  $m = 0$  modes are axisymmetric, while higher order modes vary more rapidly with longitude (see Figures 1 and 2).

### 2.2 The Linear Observational Model

The mapping from surface coefficients to any set of observations can be expressed as a linear operation:

$$\mathbf{y} = \mathcal{A}\mathbf{c} \quad (2)$$

where:

- $\mathbf{y}$  is the  $N_{\text{obs}}$ -dimensional vector of observations (e.g. flux values, photocentre positions).
- $\mathbf{c}$  is the  $(\ell_{\text{max}} + 1)^2$ -dimensional vector of spherical harmonic coefficients on the stellar surface (i.e. the set  $\{a_{\ell}^m\}$ ).
- $\mathcal{A}$  is the  $(N_{\text{obs}} \times N_{\text{modes}})$  design matrix.

This observation operator (the design matrix for an observational method) encodes the relationship between the stellar surface and measurements thereof: each element  $\mathcal{A}_{ij}$  quantifies how the  $j$ -th spherical harmonic contributes to the  $i$ -th measurement. The rows of  $\mathcal{A}$  correspond to individual measurements (e.g. flux at time  $t_1$ , astrometric position at time  $t_2$ ), while the columns correspond to the contribution of each spherical harmonic mode. The linearity of this mapping allows us to examine how the measurement geometry and rotation determine the recoverability of different modes.

### 2.3 Rank, Null Space, and Observable Information

The observation operator  $\mathcal{A}$  fundamentally determines what surface information can be recovered from measurements. To understand the information content, we can partition the spherical harmonic modes into two complementary subspaces based on their observability.

- The Rank (observable subspace): The  $R$ -dimensional subspace of modes that produce linearly independent, rotationally induced time-varying signals. These modes represent the maximum number of independent pieces of information extractable from the data alone.
- The Null Space (invisible subspace): The  $(N - R)$ -dimensional subspace of modes that produce either a constant signal, or linearly dependant signals. Any surface pattern lying in this space is invisible to the observation method.

Mathematically, the null space of  $\mathcal{A}$  is the set of coefficient vectors that satisfy:

$$\mathcal{A}\mathbf{c} = \mathbf{0} \quad (3)$$

These are linear combinations of spherical harmonic coefficients that produce no observable signal. As originally pointed out by Russell (1906), any combination of odd- $\ell$  harmonics would be a valid coefficient vector for the photometric observation operator  $A_{\text{phot}}$ . Any surface containing null space modes can, at best, only be partially recovered. The observable components may be constrained, but the null

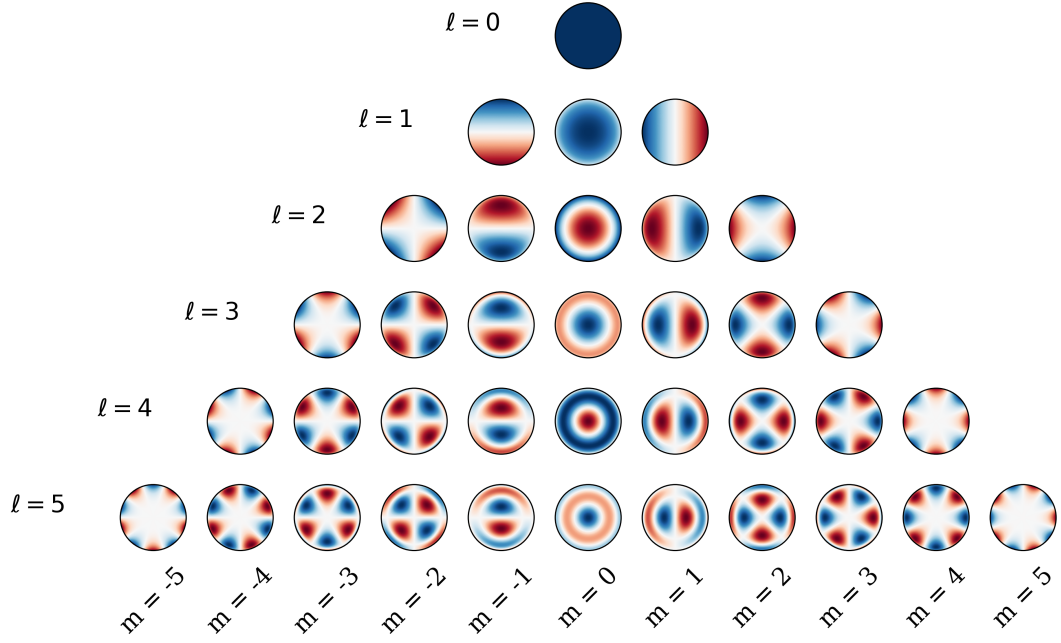


**Figure 1.** All spherical harmonic modes up to and including degree five, viewed pole on.

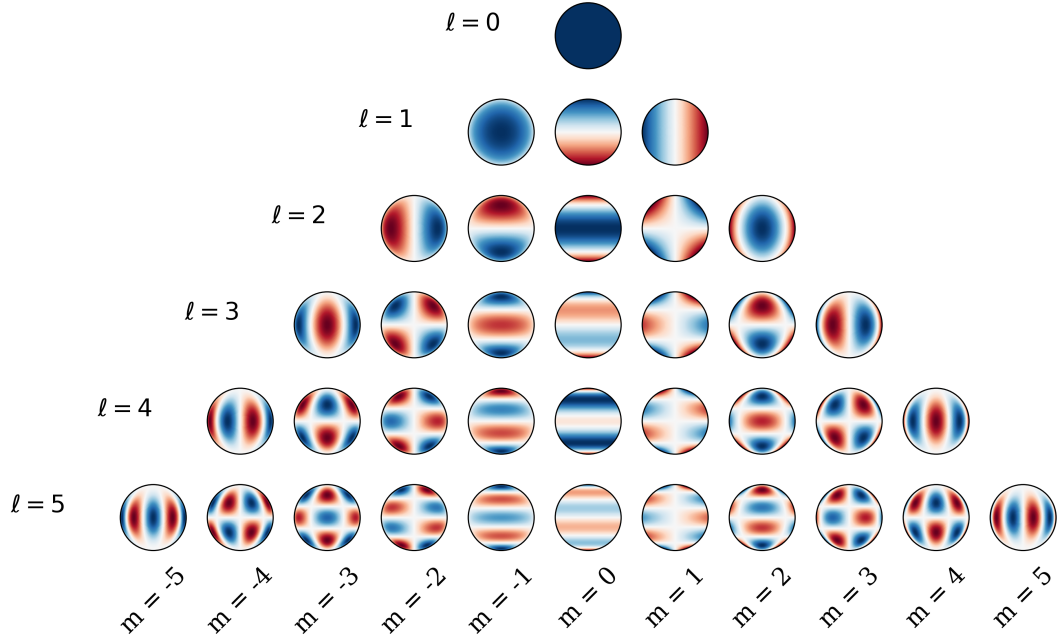


**Figure 2.** All spherical harmonic modes up to and including degree five, viewed equatorially.

space components remain undetermined regardless of measurement precision. That is to say, this is a fundamental, information-theoretic limit. Any constraints of the null modes only then only reflect prior information.

Although the spherical harmonics themselves form a complete and

orthogonal basis on the sphere, their projections through observational operators need not remain linearly independent. Consequently, the specific set of modes that span the observable (rank) subspace is not unique. One could, in principle, construct an alternative basis spanning the same subspace that yields identical observables but a vi-

sually different surface representation. Alternative bases for practical reconstruction are discussed in Section 6.5.

## 2.4 The Photometric Observation Operator

For photometry, the observable  $\mathcal{A}_{\text{phot}}$  is the integrated flux over the visible hemisphere:

$$\mathcal{A}_{\text{phot}}(Y_\ell^m, \phi_t) = \iint_{\text{visible}} I_\ell^m(\theta, \varphi) \cdot \cos \gamma \cdot \sin \theta d\theta d\varphi \quad (4)$$

where  $\cos \gamma$  is the foreshortening factor (see Appendix A2),  $\theta_{\text{obs}}$  is the observer's inclination angle,  $\phi_t$  is the rotation phase, and  $\sin \theta d\theta d\varphi$  is the surface area element / Jacobian. For a surface described by a single spherical harmonic, the photometric signal is

$$\mathcal{A}_{\text{phot}}(Y_\ell^m, \phi_t) = \iint_{\text{visible}} Y_\ell^m(\theta, \varphi) \cdot \cos \gamma \cdot \sin \theta d\theta d\varphi \quad (5)$$

Following the analysis of Luger et al. (2021), the photometric operator exhibits strong selection rules that severely limit the observable modes:

- Odd degree modes with  $\ell > 1$  are always in the null space. These modes are antisymmetric about the equator and integrate to zero regardless of viewing angle or rotation phase.
- Only even degree modes can contribute to the rank. However, not all even modes are linearly independent after integration.
- The  $m = 0$  modes are axisymmetric and never produce time-varying signals. They are thus relegated to the null space.

As Luger et al. (2021) proved, the rank of the photometric operator grows approximately as  $2\ell + 1$  for even values of  $\ell$ . Given that the space spanned by spherical harmonics grows as  $\ell^2$ , the nullity of the photometric operator also grows as  $\ell^2$ . The growth of the nullity implies that almost all of the spatial information at small scales is in the null space. In Section A4, we will demonstrate an evaluation of this integral to derive the result that all odd  $\ell \geq 3$  modes are in the null space of the photometric operator.

## 2.5 The Astrometric Observation Operator

For astrometry, the observable operator  $\mathcal{A}_{\text{astrom}}$  is the photocentre (flux weighted position) position on the sky. Dropping the normalisation factor (which is simply Equation 5), this is:

$$\mathcal{A}_{\text{astrom}}(Y_\ell^m, \phi_t) = \begin{bmatrix} X_c \\ Y_c \end{bmatrix} \quad (6)$$

$$= \iint_{\text{visible}} \begin{bmatrix} x \\ y \end{bmatrix} Y_\ell^m(\theta, \varphi) \cdot \cos \gamma \cdot \sin \theta d\theta d\varphi \quad (7)$$

where  $(x, y)$  are the projected sky coordinates, and  $[X_c, Y_c]$  are the coordinates of the photocentre. For a point at  $(\theta, \varphi)$  on the rotating star viewed from inclination  $\theta_{\text{obs}}$ :

The astrometric operator differs from the photometric operator in two notable ways: (1) It is a two-dimensional observable (at least in general, astrometric missions using relative astrometry may be limited to a one-dimensional projection of the two-dimensional signal), with each direction sampling different surface information. (2) Odd  $\ell \geq 3$  modes are accessible via astrometry (see Section 3). While odd modes with  $\ell > 1$  integrate to zero in photometry due to their antisymmetry, the position-weighting in astrometry breaks this symmetry. The multiplication by position co-ordinates  $(x, y)$  before integration means that antisymmetric intensity patterns can produce non-zero photocentre shifts. An example astrometric signal can be seen in Fig 3

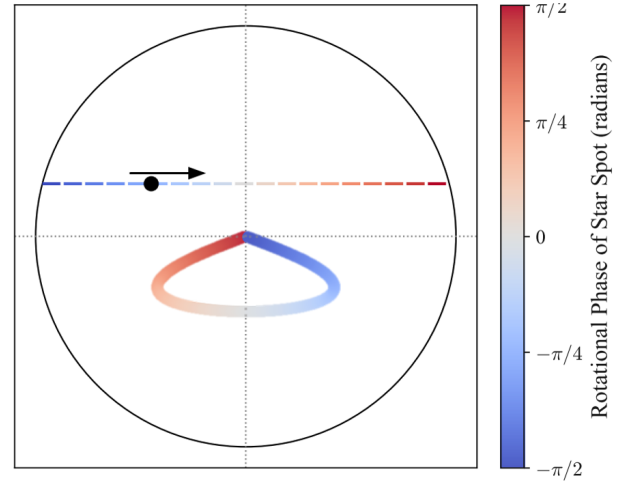


**Figure 3.** A diagram of the shape of the photometric deflection caused by a single starspot rotating at a constant rate across a stellar disk, from  $-\pi/2$  (left limb / bluer) to  $+\pi/2$  (right limb / redder). The signal includes foreshortening and limb-darkening. The size of both the signal and starspot are not to scale.

## 3 DETECTING ODD $\ell \geq 3$ WITH ASTROMETRY

A large number of spherical harmonics are invisible to photometry. Among these include all odd spherical harmonics modes with degree  $\ell \geq 3$ , as shown by Russell (1906). For completeness, we will restate the photometric result — broadly following the method in Russell (1906) — in Section A4. In this section we will demonstrate that astrometry can access some of these odd spherical harmonic modes, starting from Equation 7. Using the Cartesian to spherical coordinate transform, we can write:

$$x = \sin \gamma \cos \lambda \quad (8)$$

$$y = \sin \gamma \sin \lambda \quad (9)$$

Focusing on the  $x$ -component portion, we can write:

$$X_c = \int_0^{2\pi} \int_0^{\pi/2} [\sin \gamma \cos \lambda] Y_\ell^m(\gamma, \lambda) \cos \gamma \sin \gamma d\gamma d\lambda \quad (10)$$

now let  $u = \cos \gamma$ ,  $du = -\sin \gamma d\gamma$ , and hence  $\sin \gamma = \sqrt{1 - u^2}$ . The integral then becomes:

$$X_c = - \int_0^{2\pi} \int_0^1 u \sqrt{1 - u^2} Y_\ell^m(u, \lambda) \cos \lambda du d\lambda \quad (11)$$

Note that:

$$Y_\ell^m(u, \lambda) = c_n P_\ell^{|m|}(u) e^{im\lambda} \quad (12)$$

$$X_c = - \int_0^{2\pi} \int_0^1 u \sqrt{1 - u^2} c_n P_\ell^{|m|}(u) e^{im\lambda} \cos \lambda du d\lambda \quad (13)$$

$$X_c = - \int_0^{2\pi} e^{im\lambda} \cos \lambda d\lambda \int_0^1 P_\ell^{|m|}(u) u \sqrt{1 - u^2} c_n du \quad (14)$$

note that  $\cos \lambda$  can be written as follows:

$$\cos \lambda = \frac{1}{2}(e^{i\lambda} + e^{-i\lambda}) \quad (15)$$

The first integral above now becomes:

$$\propto \frac{1}{2} \int_0^{2\pi} (e^{i(m+1)\lambda} + e^{i(m-1)\lambda}) d\lambda = \pi(\delta_{(m,1)} + \delta_{(m,-1)}) \quad (16)$$

Above,  $\delta$  is the Kronecker delta, indicating that Eq. (13) is only non-zero when  $m = \pm 1$ . Physically, this means that only the  $m = \pm 1$  spherical harmonic components contribute to the astrometric signal. When the star rotates, the longitude coordinate transforms as  $\lambda \rightarrow \lambda - \phi$ , where  $\phi$  is the stellar rotation phase. Substituting this into the spherical harmonic term  $e^{im\lambda}$  introduces an additional factor  $e^{-im\phi}$  that survives the  $\lambda$ -integration. For the surviving  $m = \pm 1$  components, this becomes  $e^{\mp i\phi}$ , corresponding to a sinusoidal variation of the photocentre position with rotation phase. The integral then becomes:

$$X_c = -\pi \int_0^1 u \sqrt{1-u^2} P_\ell^{|m|}(u) du \quad (17)$$

Now, one of the definitions of the associated Legendre polynomials states that the following relationship exists:

$$P_\ell^{|m|}(x) = (-1)^m (1-x^2)^{m/2} \frac{d^m}{dx^m} P_\ell(x) \quad (18)$$

This means that:

$$P_\ell^{[1]}(u) = -\sqrt{1-u^2} \frac{d}{du} P_\ell(u) \quad (19)$$

so now Eq (17) becomes:

$$= \pi \int_0^1 u(1-u^2) \frac{d}{du} P_\ell(u) du \quad (20)$$

If we now integrate by parts, we can rewrite the above as:

$$= \pi(u(1-u^2)P_\ell(u))|_0^1 + \int_0^1 P_\ell(u)(1-3u^2)du \quad (21)$$

The leftmost term evaluates to zero. If we note that  $P_2(u) = \frac{1}{2}(3u^2 - 1)$ , we can rewrite the above integral as:

$$= -2\pi \int_0^1 P_\ell(u)P_2(u)du \quad (22)$$

Note that the Legendre polynomials satisfy the following relationship:  $P_\ell(-x) = (-1)^\ell P_\ell(x)$ . That is to say, that if  $\ell$  is even then  $P_\ell(u)$  is even, and if  $\ell$  is odd then  $P_\ell(u)$  is odd. Likewise, if  $\ell$  is odd, as is the case that we are interested in, then Eq (22) is also odd. Since the limits of Eq (22) are not symmetric, then, in general Eq (22) will not be zero. This however, does not suffice in showing that an odd spherical harmonic can be detected via astrometry — it could be the case that Eq (22) does evaluate to zero, but not due to the fact that it is an odd function. Hence, we need to demonstrate that there exists at least one odd  $\ell$  that does not set Eq (22) to zero. Let's set  $\ell = 3$ . Note that:

$$P_3(u) = \frac{1}{2}(5u^3 - 3u) \quad (23)$$

$$P_2(u) = \frac{1}{2}(3u^2 - 1) \quad (24)$$

Hence, Eq (22) becomes the simple integral:

$$= -\frac{\pi}{2} \int_0^1 (5u^3 - 3u)(3u^2 - 1)du \quad (25)$$

$$= -\frac{\pi}{2} \int_0^1 (15u^5 - 14u^3 + 3u)du \quad (26)$$

$$= -\frac{\pi}{4} \neq 0 \quad (27)$$

Hence, there exists at least one odd spherical harmonic that is detectable via astrometry. Note that along the way we have dropped some normalisation constants, so this is correct up to a constant (non-zero) factor. We can expand this result by solving Eq (22) more generally. By the first equation in Carlitz (1961), we can state:

$$P_\ell(u)P_2(u) = \sum_{r=0}^2 \frac{A_r A_{\ell-r} A_{2-r}}{A_{\ell+2-r}} \frac{2\ell - 4r + 5}{2\ell - 2r + 5} P_{\ell-2r+2}(u) \quad (28)$$

where

$$A_r = \frac{(2r-1)!!}{r!} \quad (29)$$

where  $n!!$  is the double factorial. The summation in Eq (28) can be expanded and applied to Eq (22):

$$\propto a \int_0^1 P_{\ell+2}(u)du + b \int_0^1 P_\ell(u)du + c \int_0^1 P_{\ell-2}(u)du \quad (30)$$

Here,  $a$ ,  $b$ , and  $c$  take the following form:

$$a = \frac{3}{2} \frac{(\ell+2)(\ell+1)}{(2\ell+3)(2\ell+1)}$$

$$b = \frac{\ell(\ell+1)}{(2\ell-1)(2\ell+3)} \quad (31)$$

$$c = \frac{3}{2} \frac{\ell(\ell-1)}{(2\ell-1)(2\ell+1)}$$

We can now use Eq (11) in Ciftja (2022) which states:

$$\int_0^1 P_{2k+1}(u)du = \frac{(-1)^k}{2^{2k+1}} \frac{(2k)!}{(k!)^2} \quad (32)$$

Note that this result only holds for  $P_\ell(u)$  when  $\ell$  is odd, which is the case here. We can then apply Eq (32) to Eq (30) and use  $\ell = 2k+1$  to obtain the following three terms:

$$\int_0^1 P_{\ell+2}(u)du = \frac{1}{2^{4(k+2)}} \frac{(2k+2)(2k+1)(2k)(2k-1)}{(k+1)^2 k^2} [...]$$

$$\int_0^1 P_\ell(u)du = \frac{-1}{2^2(k+1)} \frac{(2k)(2k-1)}{k^2} [...] \quad (33)$$

$$\int_0^1 P_{\ell-2}(u)du = \frac{1}{k} [...]$$

All three terms have [...] in common, where

$$[...] = \frac{(-1)^{k-1}}{2^{2k-1}} \frac{(2k-2)!}{((k-1)!)^2} \quad (34)$$

As we need to demonstrate that Eq (30)  $\neq 0$ , the above term is divided out. Note that due to the  $(-1)^k$  term in Eq (32), the terms in Eq (30) will have alternating signs, making it plausible that these terms cancel out. By substituting Eq (31) and (33) into (30) and simplifying, we are left with:

$$2k+1 \neq 0 \quad (35)$$

This implies that for all odd  $\ell \geq 3$ , Eq (22) is not equal to zero. Finally, this implies that for all odd spherical harmonics, there exists at least one mode that produces a detectable signal under the astrometry operator.

### 3.1 The Fisher Information Matrix

To quantify how well spherical harmonic coefficients can be constrained from observations, we use the Fisher Information Matrix

(FIM; Fisher 1935). For our linear model with Gaussian uncertainties with variance  $\sigma^2$ , the FIM takes the form:

$$\mathcal{F} = \frac{1}{\sigma^2} \mathcal{A}^T \mathcal{A} \quad (36)$$

The FIM encodes the curvature of the likelihood surface, meaning that modes with large eigenvalues are well constrained, while zero (or in our case, numerically small) eigenvalues correspond to null space modes. One benefit of the FIM formalism is that FIMs are additive if the observations are independent so that the uncertainties are uncorrelated. If we have both photometric and astrometric observations with design matrices  $\mathcal{A}_{\text{phot}}$  and  $\mathcal{A}_{\text{astrom}}$ , the combined FIM is:

$$\mathcal{F}_{\text{combined}} = \mathcal{F}_{\text{phot}} + \mathcal{F}_{\text{astrom}} \quad (37)$$

$$= \frac{1}{\sigma_{\text{phot}}^2} \mathcal{A}_{\text{phot}}^T \mathcal{A}_{\text{phot}} + \frac{1}{\sigma_{\text{astrom}}^2} \mathcal{A}_{\text{astrom}}^T \mathcal{A}_{\text{astrom}} \quad (38)$$

The preceding analysis establishes selection rules governing which spherical harmonic modes are accessible to photometry and astrometry. The primary result is that, unlike photometry, astrometry can recover odd-degree modes. However, the analytical results thus far state only which degrees are broadly accessible to each method, not which specific modes within each degree, nor how well each mode can be constrained. The following section uses the FIM framework to extend this analysis numerically, determining which modes are accessible and how well they can be constrained across arbitrary viewing geometries.

## 4 NUMERICAL ANALYSIS

### 4.1 Numerical Model

Luger et al. (2021) utilise the analytical model implemented in the python package `starry` (Luger et al. 2019), which provides exact solutions for photometric light curves. Extending this framework to astrometric observables would require deriving analogous analytical expressions for the photocentre integrals, which we leave to future work. Instead, we adopt a numerical approach that, while less computationally efficient, generalises straightforwardly to any observable.

Our numerical model discretises the stellar surface using equidistant points, each assigned values from spherical harmonic basis functions. The surface is rotated to the desired orientation, the visible hemisphere is orthographically projected onto the observer's plane, and the flux and photocentre coordinates are computed by direct summation over visible points.

To create our spherical surface, we needed equispaced points to ensure that we don't need to weight points by the surface area they represent. For more than 24 points on the sphere, there is no known exact solution to this packing problem (see Musin & Tarasov 2014). We used a Fibonacci spiral packing (González 2009) as it provides a good approximate solution for general spherical surface packing methods, where each point is evenly spaced. This method avoids the polar clustering inherent in latitude-longitude grids and eliminates the need for area-weighting, as each point represents an approximately equal solid angle. We typically used 202,500 surface points (with the exception of figures, which used more points for visual fidelity), yielding an angular resolution of approximately  $6.21 \times 10^{-7}$  steradians per point, which is much finer than the characteristic scales of spherical harmonics at our typical maximum degree of  $\ell = 15$ .

To build our design matrices, we pre-calculate our harmonics for each surface point up to degree  $\ell_{\text{max}} + 3$ . Here,  $\ell_{\text{max}}$  is the maximum

harmonic degree that we would analyse. The extra three degrees act as a buffer for numerical stability. When rotating our surface across  $\varphi_t \in [0, 2\pi]$ , we chose  $N_{\text{phases}} = 2N_{\text{modes}} + 1$  to ensure the linear system is overdetermined as to prevent aliasing. Then, for each rotation phase, we would compute the visibility and foreshortening for each surface point according to the observers inclination,  $i$ . Finally, we orthographically project the visible points and numerically integrate to compute the flux and photocentre coordinates  $(X_c, X_y)$  for each phase. This process yields three design matrices:  $\mathcal{A}_{\text{phot}}$ ,  $\mathcal{A}_x$ , and  $\mathcal{A}_y$  - each of size  $(N_{\text{phase}} \times N_{\text{modes}})$ . Finally, to compute the rank and nullity of these matrices, we performed QR decomposition (described in detail in Appendix A3).

### 4.2 The Rank and Nullity of the Observation Operators

Now that we have calculated the rank for each of the observation operators, we can investigate the behaviour of the rank and nullity for each operator. Figure 4 shows the cumulative number of spherical harmonics modes accessible to each observational technique (photometry, astrometry, and photometry + astrometry) as a function of degree  $\ell$ . For all three methods, we see that the rank grows linearly with  $\ell$ . As the number of modes grows quadratically with  $\ell$ , and as the nullity is number of modes minus the rank, the nullity also grows quadratically. This is in agreement with the results of Luger et al. (2021) for photometry. A notable implication of this result, as identified by Dholakia & Pope (2025), is that the proportion of accessible modes per degree shrinks asymptotically towards zero as the degree increases. This means that the amount of information recoverable about smaller surface scales diminishes asymptotically. While all three methods grow linearly, they do so at different rates. Figure 4 demonstrates that the combined astrometric (i.e. X and Y component) line grows faster than the photometry line. This means that not only does astrometry access different modes than photometry (as shown in section 3), but it accesses more modes. Additionally, the combination of astrometry and photometry grows faster still. This means that although astrometry accesses more modes than photometry, the modes that photometry accesses are not a subset of astrometry, meaning that these two methods are complimentary to each other.

Notably, any astrometric mission inherently provides photometric data, since astrometry measures the flux-weighted photocentre. This means that any missions will have the data available to model the stellar surface reasonably well, assuming sufficient precision. Section 6 discusses how this result enables improved noise modelling and, consequently, higher-fidelity science results.

## 5 RESULTS

### 5.1 Constraints on Spherical Harmonic Coefficients

The previous section established that the rank of each design matrix grows linearly with degree  $\ell$ , while the total number grows quadratically. However, the rank count alone does not indicate how well the data can constrain individual mode coefficients. For practical surface reconstruction, what matters is not merely whether a mode is observable, but whether observations provide meaningful constraints on its amplitude. A mode may lie in the rank but be so weakly constrained that it contributes negligible information. To quantify how well a mode can be constrained, we invoke the maximum entropy principle and consider the limit of a maximally uninformative Gaussian prior. Although this limiting prior is improper, the posterior shrinkage (Betancourt 2018) remains well-defined:

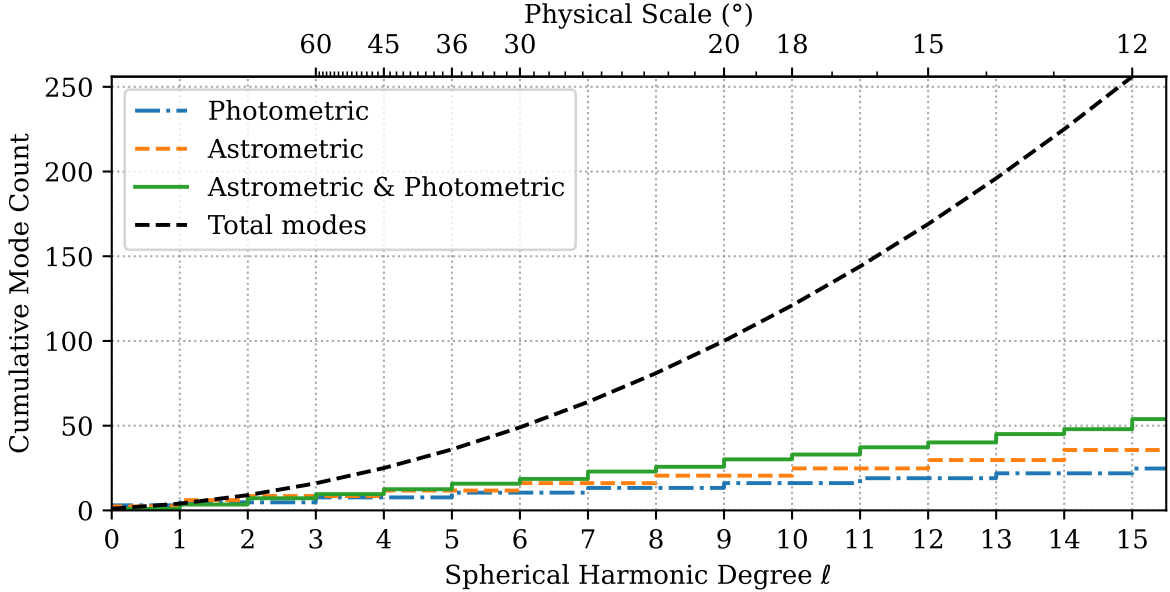


**Figure 4.** A step plot demonstrating the cumulative number of spherical harmonic modes accessible via different observing methods. The dashed black line represents the total possible number of spherical harmonic modes. The upper x axis is the characteristic scale of each spherical harmonic degree. The coloured lines represent the mean cumulative rank for each observational method across 500 inclinations, randomly sampled in  $\cos \theta_{\text{obs}}$ . The number of accessible modes increases approximately linearly with  $\ell_{\text{max}}$  for each method individually, while the combined astrometric and photometric observations recover modes at a faster rate, demonstrating that the two techniques provide complementary information.

$$S = 1 - \lim_{\sigma_0^2 \rightarrow \infty} \frac{\sigma^2}{\sigma_0^2} \quad (39)$$

Here,  $\sigma^2$  is the posterior variance and  $\sigma_0^2$  is the prior variance. Luger et al. (2021) equivalently state this as:

$$S \equiv 1 - \lim_{\lambda \rightarrow 0_+} \text{diag}(\lambda(\mathcal{A}^T \mathcal{A} + \lambda \mathbf{I})^{-1}) \quad (40)$$

If our data can exactly constrain our coefficients, the corresponding  $S$  value will be 1. If our spherical harmonic modes lie completely in the null space, then  $S$  will be 0. Hence,  $S$  is a measure of how informative a set of measurements are.

To compute the posterior shrinkage factors  $S$ , we first construct design matrices by rotating the stellar surface model through a full cycle, sampling at 720 equally-spaced rotation phases. Each column of the design matrix corresponds to one spherical harmonic mode's contribution to the observable signal over all rotation phases. Computing  $S$  via Equation 40 requires inverting the Fisher information matrix  $\mathcal{A}^T \mathcal{A}$ . However, our design matrices are rank deficient due to the substantial null spaces discussed in Section 4.2, making the Fisher matrix singular and non-invertible. To enable inversion, we add a regularization term  $\lambda \mathbf{I}$ , setting  $\lambda = 10^{-9}$  following Luger et al. (2021). This regularisation acts as a weak uninformative prior, similar to a maximum entropy prior. The finite regularisation introduces two sources of spurious non-zero shrinkage values that require careful handling. First, theoretically, in the limit  $\lambda \rightarrow 0_+$  (maximally uninformative prior), shrinkage factors  $S_{\ell,m}$  for null space modes should vanish. However, our finite  $\lambda$  produces small non-zero  $S_{\ell,m}$  values even for null modes — these do not represent genuine variance reduction from data, but rather artifacts of regularisation. Second, our numerical model introduces noise in the design matrix. While this noise is several orders of magnitude compared to the actual signal, it

can lift true null eigenvalues slightly above zero, and upon inversion, these small eigenvalues can produce inflated  $S_{\ell,m}$  values. To exclude these spurious shrinkage estimates, we implement a two-stage masking procedure. First, we mask out any design matrix columns with standard deviation below  $10^{-6}$  — the typical standard deviation of the numerical noise is less than  $10^{-7}$ . Second, we perform QR decomposition with column pivoting (detailed in Appendix A3) to identify genuinely linearly independent (LI) modes among the remaining columns. While spherical harmonics are orthogonal and hence linearly independent on the sphere, their projections through the observation operators are not necessarily LI. We set  $S_{\ell,m} = 0$  for all modes identified as null space by this procedure, ensuring that reported shrinkage values reflect only data-constrained modes.

Figure 5 presents the posterior shrinkage factor  $S$  for spherical harmonic modes up to degree  $\ell = 9$ , computed for a star viewed from the stellar equator ( $i = 90^\circ$ ). The four panels show photometry alone (top), the equatorial (X) and polar (Y) components of astrometry separately (middle two panels), and the combined photometry+astrometry case (bottom). Within each degree, modes are organised left to right as  $m = 0, 1, -1, 2, -2, \dots, \ell, -\ell$ .

This figure reveals the sparsity of the observable information: the vast majority of modes show  $S = 0$ , visually demonstrating the substantial null space discussed in Section 4.2. The modes that are observable (non-zero  $S$  values) tend to be reasonably well-constrained, with most achieving  $S > 0.5$ , with some reaching  $S \approx 1$  at low degrees. The maximum shrinkage tends to decline with increasing degree, likely representing the weakening modulation of the rotational signal from progressively smaller surface features.

The photometry panel (top, blue) shows a characteristic pattern: Non-zero values are absent from all odd degrees  $\ell > 1$ . This is a visualisation of the analytic result that all odd-mode  $\ell > 1$  lie in the null space for photometry. The astrometry panels (middle, orange)

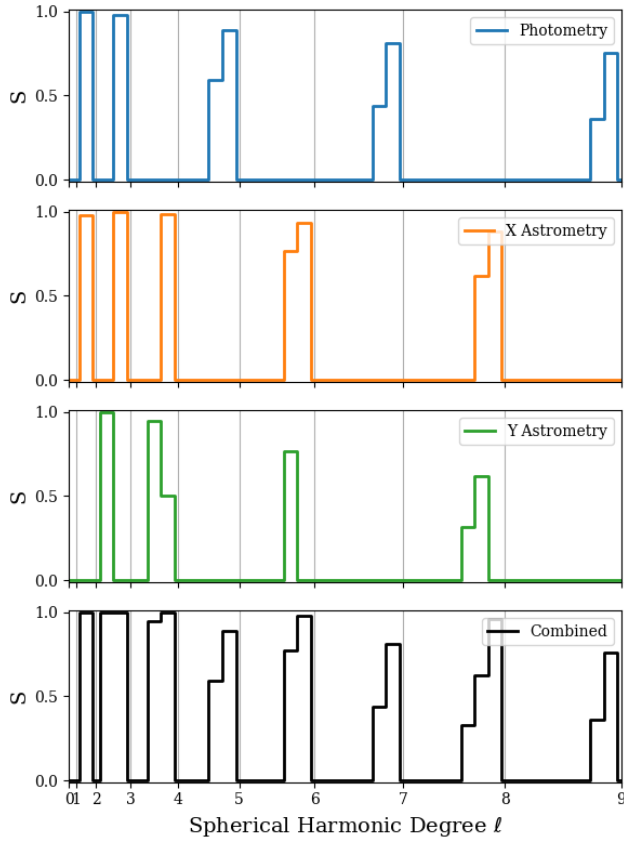


**Figure 5.** This figure shows the posterior shrinkage factors for each spherical harmonic mode, up to degree 9, for different observational methods, viewed from the stellar equator. Each mode in the degree is organised, left to right, as  $m = 0, 1, -1, 2, -2, \dots, \ell, -\ell$ . Note that for odd- $\ell$  modes, only astrometry can constrain any modes. Also note that as the degree increases, the relative number of modes with any constraint decreases.

and green) show that astrometry picks out many complementary modes to photometry. For odd degrees astrometry has non-zero  $S$  values, unlike photometry. Additionally, the X (equatorial) and Y (polar) components, while having some overlap with each other, do provide independent recovery of certain modes, i.e. each recover a different halves of the  $\ell = 2$  modes. The quadratic to linear growth of the nullity vs rank is visualised here by the approximately constant number of non-zero modes in each degree, by the growing number of zero  $S$ -value modes in each degree. In all panels of this figure, mode ( $\ell = 0, m = 0$ ) is zero. This is because this mode is uniform across the sphere, and hence does not produce a varying signal. This is the normalisation degeneracy that both [Basri \(2018\)](#) and [Luger et al. \(2021\)](#) note.

Figure 6 is similar to Figure 5, but now the y-axis of each plot is  $\cos(i)$  and the  $S$  values are represented by the colour intensity. As before, the top row represents photometry, the middle two rows are equatorial and polar astrometry, respectively, and the final row is the combination of both photometry and astrometry. The left column is zoomed into the first few degrees (up to degree  $\ell = 5$ ), while the second row shows up to degree  $\ell = 14$ . This figure demonstrates that the constraining power of each mode depends on stellar inclination — with certain modes constrained better at different inclinations. Broadly — but not monotonically, the constraining power decreases

as the star becomes increasingly pole-on. This occurs because rotational modulation arises from surface features rotating into and out of view. For near pole-on orientations, the visible hemisphere remains nearly constant throughout the rotation, producing weaker modulation and therefore weaker constraints. Additionally, which specific modes within a degree are observable changes with inclination.

## 5.2 Single Inclination Stellar Surface Map Recovery

Below we present the decomposition of several surface maps into their rank and null space components (Figures 7, 8, and 9). In each figure, the top image shows the true surface map. The left column shows the observable (rank) component, while the right shows the null-space component — features entirely invisible to observation. The first row represents the photometric operator, the middle row is the astrometric operator, and the bottom row is the represents the combined information from both the photometric and astrometric operators. Each surface in this section is viewed from an inclination of  $8^\circ$  above the equator.

### 5.2.1 Single spot case (Figure 7)

This is the simplest non-trivial test case: a single large dark spot at mid-latitude,  $30^\circ$  below the equator. This case illustrates the degeneracies affecting each technique. The photometric rank reconstruction (row 1, left), exhibits a common north-south degeneracy — the recovered surface is consistent with either a dark spot in the true hemisphere, or a mirror image dark spot reflected across the equator. This ambiguity arises because photometry cannot constrain odd- $\ell$  modes which encode hemispheric asymmetry. The limited number of  $m$  modes in the photometric rank causes noticeable location smearing.

The astrometric rank (row 2, left) shows a different degeneracy structure. It exhibits a bright/dark spot location ambiguity. The photocentre time series data is consistent with either (1) a dark spot in the true location, or (2) a bright spot at the opposite disk location ( $\approx 180^\circ$  rotation in longitude, mirrored in latitude). The degeneracy occurs because the photocentre displacement depends on both the sign and location of the flux perturbation.

The combined rank reconstruction (row 3, left) resembles the true surface much more closely than photometry or astrometry alone. The spot is localised fairly well, although there is some latitudinal smearing. The north-south photometry degeneracy is broken because the astrometry rank contains odd- $\ell$  modes encoding hemispheric asymmetry. The bright/dark spot location ambiguity present in the astrometric reconstruction is broken because the photometry requires a flux deficit, eliminating the bright region solution. The null space reconstructions of each method all closely resemble the true surface. This emphasises the still present large null space.

### 5.2.2 Multiple spot case (Figure 8)

This test presents a more complex surface: nine randomly distributed spots, some overlapping to create seven distinct dark regions. The spots span nearly the full latitudinal range, with some partially or fully outside the visible hemisphere. The photometric reconstruction (row one, left) shows severe blending and ambiguity. The north-south degeneracy causes some reflected spots to merge with real ones, while spurious dark features appear in regions that should be spotless. This reproduces the result of [Luger et al. \(2021\)](#): spot number is only weakly constrained by photometry alone.

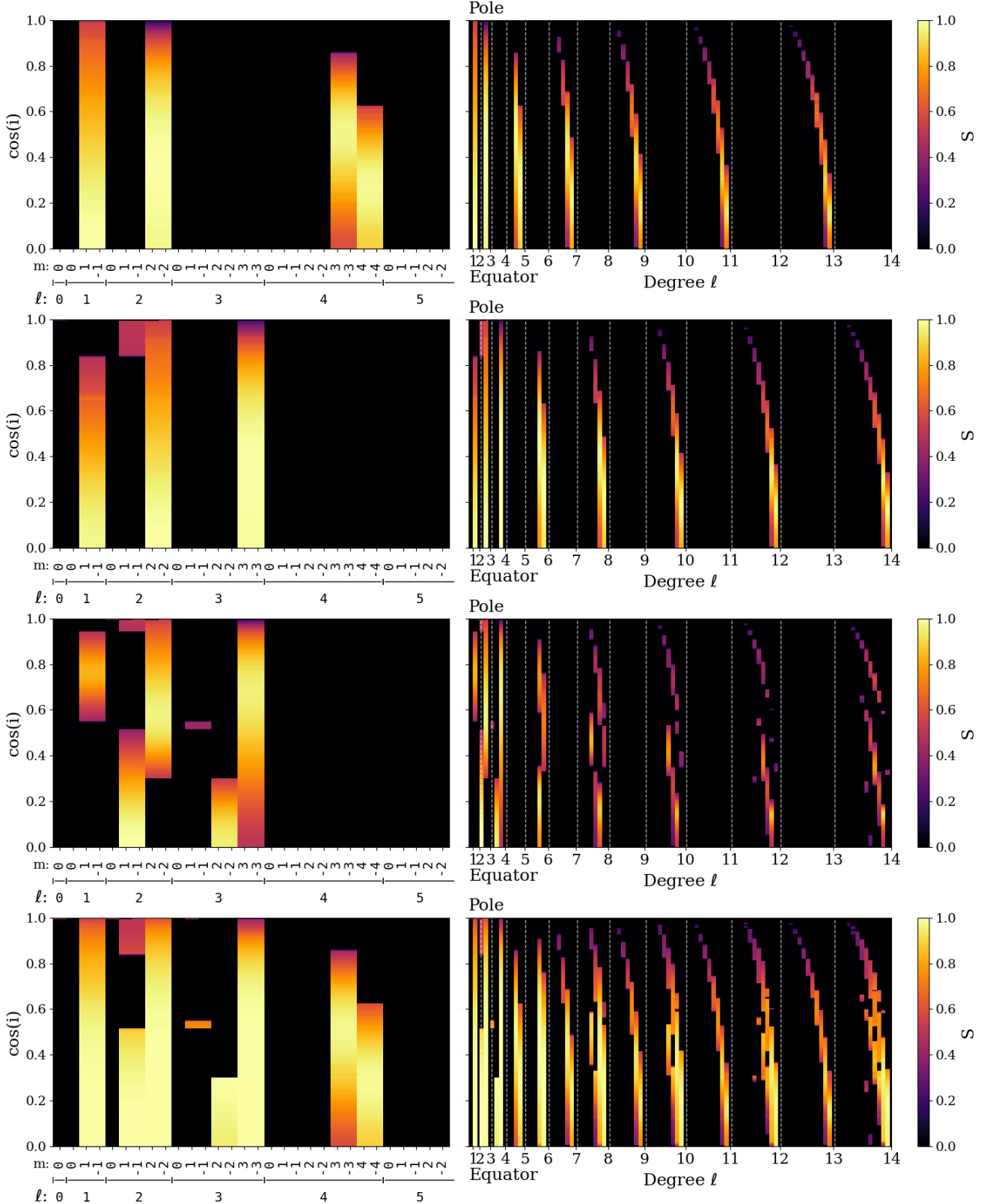


**Figure 6.** The  $S$  value for each mode across all inclinations, up to degree 5 (left) and degree 14 (right). Rows show, from top to bottom: photometry, equatorial astrometry, polar astrometry, and combined photometry and astrometry. The recoverable modes depend on inclination: as inclination increases, the recoverable modes shift towards lower  $|m|$  and the constraining power  $S$  generally decreases.

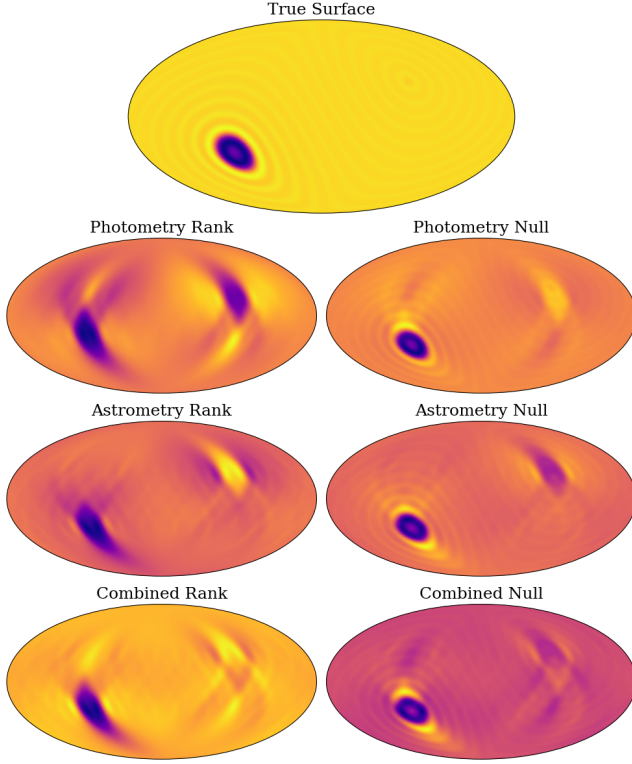


**Figure 7.** The rank and null spaces for stellar surface reconstructions. The top panel shows the true surface: a single spot created with spherical harmonics up to degree  $\ell = 30$ , viewed at inclination  $8^\circ$ . Ringing artifacts arise from the finite harmonic expansion of this sharp feature. Subsequent rows show reconstructions from the rank space (left column) and residuals in the null space (right column) for photometry alone, astrometry alone, and combined photometry+astrometry measurements. Unlike each method alone, the rank of the combined method recovers the latitude and longitude of the spot, with some smearing.

The astrometric rank reconstruction (row two, left) shows improved latitudinal discrimination compared to photometry. However, the bright/dark mirror spot degeneracy creates a complex pattern where it is hard to distinguish which features may be real from reconstruction artifacts.

The combined rank reconstruction (row two, left) fares comparably well: the five dark regions, composed of seven spots, in the middle third band of latitudes are recovered well enough to place their approximate latitudes and longitudes. The two polar spots however are not recovered well. There is large dim region in the approximate region of the northern polar spot, which demonstrates a low confidence poorly localised recovery. However, the southern polar spot is essentially invisible. The leopard-spot pattern of dark rings with bright inner regions in the combined null space reconstruction (row 3, right) come from high-frequency residuals, indicating that the large scale structure lies mostly in the observable subspace. Astrophysically, this implies that the location of the spots can be constrained, but the size of the spots can be constrained less well. This is likely due to the size-contrast degeneracy of spots.

### 5.2.3 Message case (Figure 9)

As in Luger et al. (2021), we present a deliberately challenging case: the phrase "GREETINGS EARTHLINGS" written across the entire

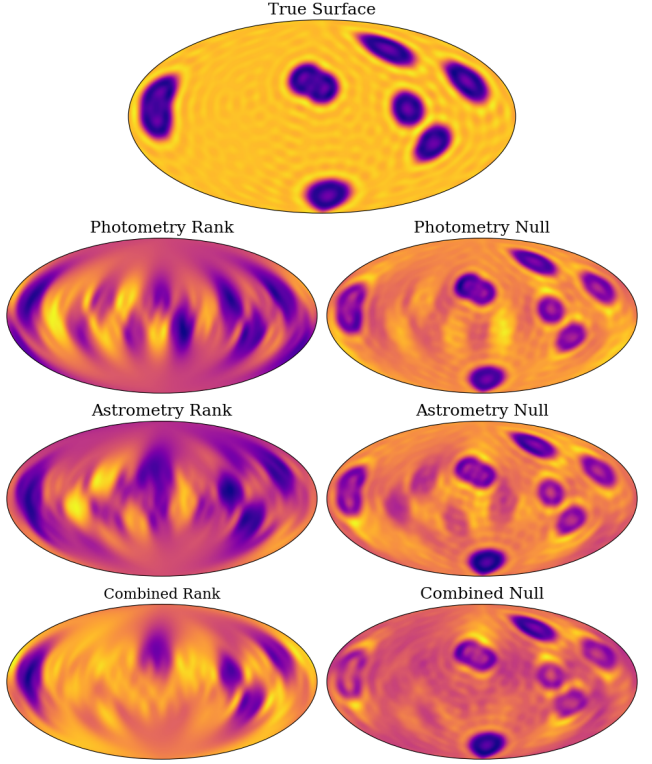


**Figure 8.** Same as Figure 7, but for nine spots randomly placed over the stellar surface, sampled from a uniform distribution. As with Figure 7, the combined rank has a better recovery, recovering five of the seven spot groups. The two spot groups that are poorly recovered are the closest to the poles.

stellar surface. Text cases like these provide good diagnostics for surface reconstruction methods because it contains both large scale structure (the overall text band) and small scale structure, such as the individual letter strokes. Text readability provides a good test against apophenia: if the reconstruction method were genuinely recovering fine surface detail rather than imposing prior-driven patterns, the text should be legible. In this case, each of the photometry, astrometry and combined ranks are all qualitatively very similar, with no text being legible at all. All that can be stated is that there appears to be a complex structure around the equatorial band.

### 5.3 Multiple Inclination Stellar Surface Map Recovery

The preceding analysis examined surfaces viewed from a single inclination ( $i = 8^\circ$ ). However, Figure 6 demonstrates that the posterior shrinkage  $S$  for individual modes varies strongly with viewing angle. Following Luger et al. (2021), if we could observe the same star from multiple inclinations simultaneously, we should achieve better surface recovery by accessing modes that lie in the null space for some single inclination.

In reality, this multi-inclination process could be approximated through ensemble analysis of many similar stars at different random inclinations. This does not mean individual surface features are recoverable from the data alone; rather, it constrains the distribution of surface properties across the population of similar stars — i.e. typical spot latitudes, spot filling factors, hemispheric asymmetries, etc. In this sense, the ensemble acts somewhat like a physical prior,



**Figure 9.** Same as Figure 7, but the message "GREETINGS EARTHLINGS" has been 'written' on the stellar surface. This message highlights the recovery efficiency of a large scale pattern, with finer details (letter strokes) spread throughout. The recovery via any method is insufficient to recover the fine structure.

replacing the uninformative maximum entropy prior with empirically derived constraints from the population itself.

As Luger et al. (2021) did, we also revisited the same surfaces as in the prior section for comparison. Figures 10, 11, and 12 are the same as the aforementioned surfaces, but they have now been observed from 8 different inclinations (sampled randomly from  $\cos(i)$  where  $i \in [0, \pi/2]$ ). Note that in all these figures, the null space exhibit zebra-stripe patterns. These are numerical artifacts arising from the finite harmonic expansion ( $\ell_{\max} = 30$ ) and the limited number of inclinations (80). They should not be treated as physical features.

### 5.3.1 Single spot, multi-inclination (Figure 10)

The photometric rank (row one, left) and astrometric rank (row two, left) are quite similar to the single inclination recovery. That is to say, the same north-south and bright/dark spot degeneracies are present. However, the spot localisation is much better, with only a very small amount of latitudinal smearing. Likewise, the combined rank (row three, left) once again breaks the degeneracies, and like the two methods individually, the combined rank has a much better spot localisation.

### 5.3.2 Multiple spots, multi-inclination (Figure 11)

The reconstruction quality shows substantial improvement over Figure 8. As with the preceding single spot case, the spot localisation shows significant improvement. More notable, however, is that the

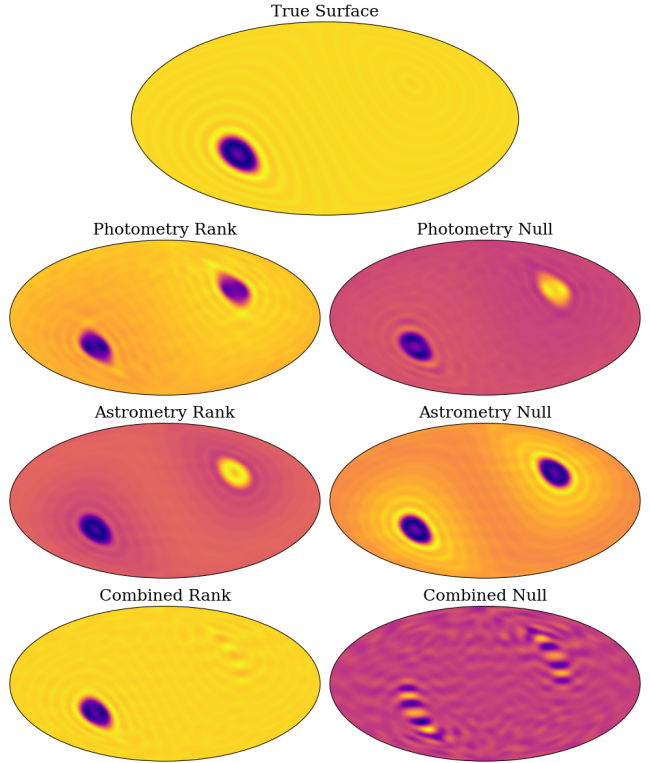


**Figure 10.** Same as Figure 7, but the surface has been observed from 8 inclinations sampled from  $\cos(\text{inclination})$ . The stripy, zebra-like pattern is an artifact arising from the limited degree used (only up to  $\ell = 30$ ). In contrast to Figure 7, there is no latitudinal smearing as the spot is very well localised.

two polar spots that were essentially invisible in the single spot case have now been recovered well. This is primarily because more of the surface has been observed, and less to do with imposing a physical prior on the reconstruction. However, the leopard-spot pattern mentioned above in the null reconstruction is essentially gone, especially in the combined rank. This improvement is due to the prior and not because more of the surface has been observed — the leopard-spot pattern was observed on spots that were always visible, so this improvement must be due to the improved prior.

### 5.3.3 Message, multi-inclination (Figure 12)

This surface presents a significant improvement. While some letter-like shapes are present in the photometry rank reconstruction, the message is still illegible. The illegibility motivates the use of such a message as a sanity check for what is actually recoverable. While the astrometry rank recovery looks more legible, it would be hard to claim with any confidence what the actual message was if the true surface was unknown.

Finally, the reconstruction of the combined rank is much better — the message is fully legible.

## 6 DISCUSSION

Our results demonstrate that astrometric time series encode independent and highly complementary information to photometric light curves. We have established the theoretical information content of

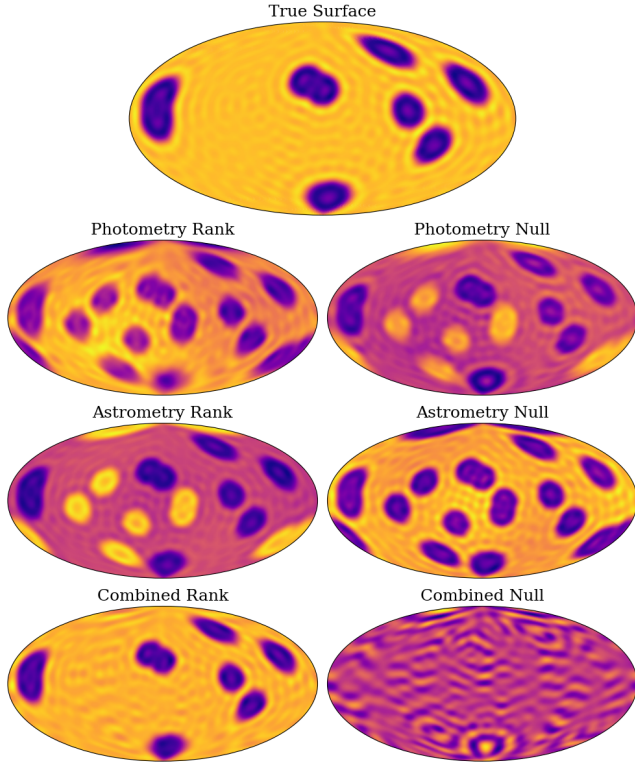


**Figure 11.** Same as Figure 10, but for nine spots randomly placed over the stellar surface, sampled from a uniform distribution. Unlike Figure 10, all seven of the seven spot groups are recovered well, with the shapes of the spots nearly recreating the true surface.

astrometric signals for the ill-posed inverse problem of stellar surface mapping. In particular, we have demonstrated that astrometry is sensitive to all dipole modes and higher-order odd spherical harmonic modes that are invisible to photometry. These modes encode north-south asymmetries on stellar surfaces, potentially allowing for the recovery of hemispheric differences in activity levels, such as persistent active-latitude belts and polar spots. By measuring the motion of the photocentre rather than the disk integrated flux, astrometry introduces a first-moment weighting that breaks several symmetries.

### 6.1 Theoretical versus Practical Recovery

The Fisher information analysis presented here establishes fundamental limits on mode observability, under ideal circumstances: infinite signal-to-noise ratio, uncorrelated Gaussian uncertainties, and complete rotational phase coverage. Real data will fall short of these ideals.

Uncertainties and systematic effects will degrade practical recovery below the limits presented here. We have established which modes are in principle recoverable, but not which remain recoverable at finite SNR. Higher-degree spherical harmonics produce progressively smaller signals: as seen in Equation A10, the amplitude is dominated by the  $1/(2^\ell \ell!)$  prefactor, which decreases rapidly with  $\ell$ . Consequently, high-degree modes are the first to fall below the noise floor. There is also a trade-off between observing cadence (better temporal sampling to avoid aliasing) and integration time (better SNR per measurement), which should be optimised for each target based on stellar rotation period, target brightness, and spot lifetime.



**Figure 12.** Same as Figure 10, but the message "GREETINGS EARTHLINGS" has been written on the stellar surface. Unlike Figure 10, the combined rank recovers the surface sufficiently well as to allow the message to be read. Photometry and astrometry alone struggle to recreate the message.

Physical effects, such as meridional flows, spot evolution, stellar oblateness, and differential rotation, violate our assumption of static, spherical, rigid body rotation. Spot lifetimes on Solar-type stars range from days to months (Hathaway & Choudhary 2008) with larger spots persisting for weeks to many months (Namekata et al. 2019). Additionally, spot evolution can mimic or obscure rotational modulation signatures (Basri 2018). Meridional flows can transport magnetic features poleward potentially introducing apparent differential rotation signatures (Vashishth & Karak 2024)

### 6.2 Astrometric Signal Structure and Exoplanet Detection

High quality modelling of stellar activity is difficult (Rackham et al. 2023, and the references therein). As such, noise from stellar activity is treated as a nuisance to be filtered out. However, many noise processes are not random, but are instead deterministic representations of the surface. In particular, astrometric jitter at the level of precision of missions like TOLIMAN is closely related to larger-scale surface incoherence on rotational timescales (Deagan et al., submitted). Not only is this signal interesting for stellar physics, but it could be better marginalised over to allow a more robust and precise extraction of any planetary signals.

Even for relative (i.e. one-dimensional) astrometric missions such as TOLIMAN or ARMADA, the rotating stellar surface samples different spherical harmonic modes as it projects onto the measurement axis at different phases. The two-dimensional photocentre signal is thus accessible from this one-dimensional projection of the two-

dimensional signal, albeit with reduced information compared to full two-axis astrometry.

Missions like TOLIMAN employ differential astrometry between binary components to avoid certain systematic errors. However, each star contributes its own activity-induced jitter, which ought to be disentangled for planet detection. For binaries with different rotation periods, temporal separation via Fourier analysis may be possible. This is more likely in wide binaries as tidal interactions are weak, so each component spins down independently via magnetic braking at a rate set by its mass. Close binaries, by contrast, tend toward tidal synchronisation, precluding this approach. Alpha Centauri is a favourable case, with a wide separation and rotation periods of  $28.3 \pm 0.5$  days for Alpha Cen A (Huber et al. 2020) and  $36.2 \pm 1.4$  days for Alpha Cen B (DeWarp et al. 2010). If the photometric signal from each component can also be separated, further constraints on individual surfaces become possible. Activity cycles present both a challenge and an opportunity. If both stars are concurrently active, disentangling their contributions is difficult. However, if one star is quiescent while the other is active, the jitter will be dominated by the active component, potentially allowing tighter constraints on its surface.

### 6.3 Limb Darkening

Thus far, our analysis has neglected limb-darkening. Luger et al. (2021) go into the impact of this in detail. They demonstrate that the inclusion of limb-darkening has a mode mixing effect — some null space modes are lifted out of the null space and gain some constraints. When limb-darkening is present, no coefficient has  $S = 0$ , and no coefficient can have  $S = 1$  — the constraint has been spread across modes. The exact mixing depends on the limb-darkening law applied, but they note that any polynomial limb-darkening law can be expressed exactly as a linear combination of the  $m = 0$  spherical harmonics up to degree equal to the order of the polynomial (Agol et al. 2020; Luger et al. 2021). We defer to their analysis for the photometric case and note that the astrometric case would follow similar principles, with the limb darkening position weighting modifying which modes are lifted from the null space.

### 6.4 Spot properties and Observable Degeneracies

A fundamental limitation of photometry and astrometry is the spot size-contrast degeneracy (Luger et al. 2021). While this degeneracy can feasibly be broken with high cadence observations as a spot rotates out of view, limb-darkening and foreshortening complicates this. Observations generally constrain only the flux deficit (contrast times area), not spot size and contrast independently. Even when a transiting exoplanet eclipsing a spot, this degeneracy is still present (Morris et al. 2017).

Multi-band observations could feasibly be a solution. Akin to multi-band observations in photometry (e.g. Gully-Santiago et al. 2017; Shapiro et al. 2021), an astrometric mission could use multiple band passes to observe the same surface. This would start to constrain spot contrast as spots are cooler than the surrounding photosphere, and contrast in the blackbody curves changes as a function of wavelength. However, high-precision astrometric missions such as TOLIMAN require long integration times for sufficient SNR (approximately one hour; Tuthill et al. 2018), making sequential multi-band observations impractical unless the instrument can observe multiple bands simultaneously. Alternatively, coordinated observations with photometric instruments such as TESS or ground-based facilities could provide the spectral constraints independently.

### 6.5 Surface Representation and Reconstruction

While this work uses spherical harmonics as a basis for analysing information content, spherical harmonics may not be optimal for actual surface reconstruction. Spherical harmonics form a smooth, global basis which, like Fourier series, struggle to represent sharp discontinuities like spot edges. Additionally, their large scale features may not be suitable for most stellar surfaces. For example, a large spot group on the Sun may have an area of 1000 micro-solar hemispheres (Baumann & Solanki 2005). This roughly corresponds to a circular spot with a diameter of about  $5^\circ$ , which would correspond to a spherical harmonic degree of at least  $\ell = 36$ . Flares, having much smaller sizes, would be harder to model using spherical harmonics. Furthermore, there is no natural way to enforce physical constraints, like the non-negativity of intensity. Alternative representations could prove more effective for practical mapping.

Discretised pixel grids are frequently used in stellar surface mapping, where the stellar surface is divided into a dense tessellation of pixels whose intensities are inferred through inversion (e.g. Harmon & Crews 2000; Roettenbacher et al. 2017). These approaches are conceptually simple and allow for flexible surface geometries, but they are computationally intensive and typically require regularisation technique to reduce degeneracies and stabilise the inversion.

Parametric spot models (e.g. Davenport et al. 2015; Morris et al. 2017) directly fit spot properties (latitude longitude, size, contrast) rather than using a set of basis functions. These have the benefit of easily allowing enforcement of physical priors (spot temperature, compactness, size distribution, etc.), however, they often assume circular or elliptical spot geometry which limits their realism.

Spherical wavelets (Price et al. 2021, 2024) provide localised, multi-scale decomposition suited to localised features with sharp boundaries. Sparsity priors can also be enforced. Slepian functions (spatially concentrated eigenfunctions of the spherical harmonic basis) can focus information into a region of interest while maintaining orthogonality, potentially improving reconstruction of localised features (Khalid et al. 2016; Michel & Simons 2017; Roddy & McEwen 2022).

While this work, like Luger et al. (2021), analyses theoretical information recoverability under maximally uninformative priors, realistic surface reconstruction can leverage substantial prior knowledge. Solar observations can provide detailed empirical constraints on spot properties such as size distributions, temperature contrasts, preferred latitudes and lifetimes. Stellar models impose thermodynamic and electromagnetic constraints on permissible surface configurations. Large photometric surveys, such as Kepler and TESS, reveal population-level statistics about activity patterns across spectral types and ages (e.g. Montet et al. 2017). These physically motivated priors can substantially improve practical surface recovery beyond the fundamental limits established here. This work, however, should be understood to be in the context of uninformative priors.

### 6.6 Ensemble Observations and Population Constraints

While individual stellar surfaces remain substantially unconstrained due to large null spaces (see Figure 4), ensemble observations across many stars at random inclinations can constrain population-level properties (Luger et al. 2021). As Figure 6 shows different inclinations render different modes observable. Averaging over an ensemble samples many different observable subspaces, collectively accessing more modes than any single inclination. This approach does not recover individual surface features but can constrain statistical properties, such as spot filling factors, but also from odd  $\ell$  modes typical

spot latitudes and hemispheric asymmetries could be recovered. For areas such as dynamo theory, where individual features aren't important but collective feature such as active latitudes are important (Berdugina 2005, and the references therein), this population level characterisation could be helpful.

## 6.7 Potential Immediate Applications: Evolved Giants with Gaia

Sun-like stars are challenging targets requiring new, sub-microarcsecond precision instruments. Evolved giants, however, potentially offer more immediate opportunities for astrometric surface mapping with existing technology. With the upcoming release of Gaia DR4, which will provide  $\lesssim 10\mu\text{as}$  micro-arcsecond precision on average position for bright stars (Brown 2025), evolved giants present three advantages: (1) Their larger radii produce proportionally large photocentre displacements, (2) they can harbour large, long lived spots (Strassmeier 1999) and (3) low surface gravity drives large scale convective flows such as giant convective cells (Chiavassa et al. 2011; Paladini et al. 2017; Vlemmings et al. 2024) that would produce large, persistent astrometric signals (Ludwig 2005).

## 7 CONCLUSIONS

In this work we extended the theoretical framework introduced by Luger et al. (2021) to quantify the information content of astrometric observations in addition to photometric observations in the context of the inverse problem of stellar mapping. We demonstrated that astrometry accesses complimentary surface information that is invisible to photometry alone. We have demonstrated analytically that astrometry can constrain odd degree ( $\ell \geq 3$ ) spherical harmonic modes that encode hemispheric asymmetries. We have shown that like photometry, the number of recoverable harmonics grows linearly (and faster than the photometric case), and have demonstrated that despite this, the nullity still grows quadratically, implying that the fraction of recoverable modes shrinks asymptotically toward zero as  $\ell$  increases. We also demonstrated strong inclination dependence, with constraints weakening towards pole-on orientations (although, not monotonically). Finally, we discussed applications where this work could be useful as well as demonstrating surface recovery for several illustrative surfaces.

These results establish theoretical limits on stellar surface information recovery under ideal conditions with uninformative priors. Practical recovery will fall short of these limits due to noise, finite sampling, and systematics such as surface evolution. However, physically motivated priors in addition to empirically derived priors can substantially improve surface reconstruction beyond what the data technically constrains.

Impending applications exist for evolved giant stars, where Gaia DR4 astrometry may enable insights regarding large scale surface structures. For Sun-like stars, forthcoming sub-microarcsecond missions (TOLIMAN, CHES, ARMADA, etc) will provide the required precision for activity characterisation that will be beneficial to exoplanetary science, as well as auxiliary stellar physics science goals.

Understanding stellar surfaces through multiple techniques — photometry, Doppler imaging, Zeeman Doppler imaging, interferometry, and now astrometry — is important for ensuring interoperability between techniques and enabling orthogonal measurements of stellar surfaces. One benefit is to better characterise exoplanet host stars in terms of noise. However, caution still needs to be heeded.

As Roettenbacher et al. (2017) demonstrates, independent reconstructions from different techniques can yield substantially different results. Astrometry, especially in tandem with photometry, provides new constraints that can reduce degeneracies that exist in stellar surface mapping.

## ACKNOWLEDGEMENTS

We would like to thank Dr Jamila Taaki for helpful discussions that improved this manuscript. Additionally, we would like to thank Dr Benjamin Pope for helpful discussions regarding some of the mathematics presented in Section 5.1 of this work.

Parts of this work were developed within the Stellar and Planetary Research in Greater Sydney (SPRIGS) meeting series.

This research includes computations using the computational cluster Katana supported by Research Technology Services at UNSW Sydney (PVC (Research Infrastructure), UNSW Sydney 2010).

## DATA AVAILABILITY

No data was taken in order to create this paper. Code used to generate figures and results can be provided upon reasonable request.

## APPENDIX A: MATHEMATICAL DERIVATIONS

### A1 Alternative form of Spherical Harmonics

Spherical harmonics are usually defined as such:

$$Y_\ell^m(\theta, \varphi) = \sqrt{\frac{2\ell+1}{4\pi} \frac{(\ell-|m|)!}{(\ell+|m|)!}} P_\ell^m(\cos \theta) e^{im\varphi} \quad (\text{A1})$$

where  $P_\ell^m$  are the associated Legendre polynomials defined as:

$$P_\ell^m(x) = \frac{(-1)^{|m|}}{2^\ell \ell!} (1-x^2)^{|m|/2} \frac{d^{\ell+|m|}}{dx^{\ell+|m|}} (x^2-1)^\ell \quad (\text{A2})$$

Note that regular Legendre polynomials are simply when the above equation has  $m = 0$ . The higher order differentiation can be tedious to solve for a given  $(\ell, m)$ . Following the description in Mulder (2000), we can convert this high order differentiation to a summation as follows. Note that using the binomial theorem we can write:

$$\frac{d^{\ell+|m|}}{dx^{\ell+|m|}} (x^2-1)^\ell = \frac{d^{\ell+|m|}}{dx^{\ell+|m|}} \left[ \sum_{k=0}^{\ell} \binom{\ell}{k} (x^2)^{\ell-k} (-1)^k \right] \quad (\text{A3})$$

$$= \sum_{k=0}^{\ell} (-1)^k \binom{\ell}{k} \frac{d^{\ell+|m|}}{dx^{\ell+|m|}} [x^{2\ell-2k}] \quad (\text{A4})$$

Note that for the differentiation term in A4, we have the following cases:

$$\frac{d^{\ell+|m|}}{dx^{\ell+|m|}} x^{2\ell-2k} = 0 \text{ if } \ell + |m| > 2\ell - 2k \quad (\text{A5})$$

$$\Rightarrow = 0 \text{ if } k > \lfloor \frac{\ell-|m|}{2} \rfloor \quad (\text{A6})$$

Note  $\lfloor (l-|m|)/2 \rfloor$  refers to the largest integer  $\leq (l-|m|)/2$ . In the other case, where  $l+|m| \leq 2\ell - 2k$ , we have:

$$\begin{aligned} \frac{d^{\ell+|m|}}{dx^{\ell+|m|}} x^{2\ell-2k} &= (2\ell-2k)(2\ell-2k-1)\dots \\ &\quad \times (2\ell-2k-(\ell+|m|)+1)x^{2\ell-2k-(\ell+|m|)} \\ &= \frac{(2\ell-2k)!}{(\ell-|m|-2k)!} x^{\ell-|m|-2k} \end{aligned} \quad (\text{A7})$$

Thus we can rewrite Equation (A2) as:

$$P_\ell^m(x) = \frac{1}{2^\ell \ell!} (1-x^2)^{|\ell|/2} \sum_{k=0}^{\lfloor \frac{\ell-|m|}{2} \rfloor} (-1)^{|m|+k} \binom{\ell}{k} \frac{(2\ell-2k)!}{(\ell-|m|-2k)!} x^{\ell-|m|-2k} \quad (\text{A8})$$

Now we can write the following, noting that we have used the trigonometric identity of  $\sin^2 \theta + \cos^2 \theta = 1$ :

$$\begin{aligned} P_\ell^m(\cos \theta) &= \frac{1}{2^\ell \ell!} \sin^{|m|} \theta \\ &\times \sum_{k=0}^{\lfloor \frac{\ell-|m|}{2} \rfloor} (-1)^{|m|+k} \binom{\ell}{k} \frac{(2\ell-2k)!}{(\ell-|m|-2k)!} \cos^{\ell-|m|-2k} \theta \end{aligned} \quad (\text{A9})$$

hence:

$$\begin{aligned} Y_\ell^m(\theta, \varphi) &= e^{im\varphi} \frac{1}{2^\ell \ell!} \sqrt{\frac{2\ell+1}{4\pi} \frac{(\ell-|m|)!}{(\ell+|m|)!}} \sin^{|m|} \theta \\ &\times \sum_{k=0}^{\lfloor \frac{\ell-|m|}{2} \rfloor} (-1)^{|m|+k} \binom{\ell}{k} \frac{(2\ell-2k)!}{(\ell-|m|-2k)!} \cos^{\ell-|m|-2k} \theta \end{aligned} \quad (\text{A10})$$

This form of spherical harmonics can be easier to work with when calculating the rank and nullity of different observable operators.

## A2 Derivation of Foreshortening Factor

In future appendices, we will solve integrals which require a foreshortening factor. This factor is derived here.

The foreshortening factor is defined as:

$$\cos(\gamma) = \hat{n} \cdot \hat{o} \quad (\text{A11})$$

where  $\hat{n}$  is the surface normal of point  $(\theta, \varphi)$  on the star and  $\hat{o}$  is the direction from the centre of the star to the observer. From the observers reference frame, we have:

$$\hat{n}(t) = \begin{bmatrix} \sin \theta \cos(\varphi_0 + \phi_t) \\ \sin \theta \sin(\varphi_0 + \phi_t) \\ \cos \theta \end{bmatrix} \quad (\text{A12})$$

and

$$\hat{o}(t) = \begin{bmatrix} \sin \theta_{\text{obs}} \cos \varphi_{\text{obs}} \\ \sin \theta_{\text{obs}} \sin \varphi_{\text{obs}} \\ \cos \theta_{\text{obs}} \end{bmatrix} \quad (\text{A13})$$

Without loss of generality, we set  $\varphi_{\text{obs}} = 0$  and take the dot product to obtain:

$$\cos(\gamma) = \sin \theta \sin \theta_{\text{obs}} \cos(\varphi - \phi_t) + \cos \theta \cos \theta_{\text{obs}} \quad (\text{A14})$$

## A3 Numerical Rank determination via QR decomposition

Unlike the work done in Luger et al. (2021), where an analytical model for photometric light curves was used (see Luger et al. 2019), we did not create an analytical model for astrometric signals and instead used a numerical model. To ensure the accuracy of our Rank-Nullity analysis, we performed QR decomposition.

To determine which spherical harmonic modes are detectable under a specific operator, we need to find the rank and null space of the

design matrix  $\mathcal{A}$ . Direct computation of the rank via Gaussian elimination or singular value decomposition (SVD) can be numerically unstable, especially for large matrices with near-dependencies. Instead we employ QR decomposition with column pivoting for numerical stability, described below:

$$\mathcal{A}P = QR \quad (\text{A15})$$

where  $P$  is a permutation matrix that rearranges the columns of  $\mathcal{A}$  in descending order of the magnitude of  $R_{ii}$ . Here:

- $Q$  is an  $(m \times n)$  matrix with orthonormal columns that form a basis for the column space of  $\mathcal{A}$
- $R$  is an  $(n \times n)$  upper triangular matrix that maps between the columns of  $\mathcal{A}P$  and  $Q$

The  $Q$  matrix is constructed iteratively through the Gram-Schmidt process:

- Normalise the first column of  $\mathcal{A}$  to obtain the first column of  $Q$  ( $q_1$ )
- Take the second column of  $\mathcal{A}$ , subtract its projection onto  $q_1$  and normalise the residual to obtain  $q_2$
- For the  $j$ -th column of  $\mathcal{A}$ , subtract its projections onto all previously constructed basis vectors  $q_1, \dots, q_{j-1}$  and normalise the residual to obtain  $q_j$

Each entry of  $R$  encodes the overlap between an original column of  $\mathcal{A}$  and the orthogonal basis of  $Q$ :

$$R_{ij} = q_i^T a_j \quad \text{for } i \leq j \quad (\text{A16})$$

The diagonal entries capture the size of the new, independent contribution/direction:

$$R_{jj} = \left\| a_j - \sum_{i=1}^{j-1} (q_i^T a_j) q_i \right\| \quad (\text{A17})$$

If  $R_{jj}$  is large, the column introduces a genuine new direction in the span (i.e., new information). Conversely, if  $R_{jj}$  is small, this column is almost entirely explained by previous columns and belongs to the null space. Any size/length originates from numerical noise and is not a genuine new direction in the span. The  $P$  matrix reorders the columns of  $\mathcal{A}$  such that the diagonal of  $R$  is decreasing in magnitude — this typically creates a cliff when  $R_{jj}$  is plotted, allowing for the separation of the rank and null columns. Given our surface resolution, we typically set the Rank/Null cut off at  $10^{-6} \times |R_{00}|$  (see Fig A1).

## A4 Proof that Photometry Cannot Access Odd $\ell \geq 3$

We can start by stating that the surface of a star can be described by the function  $B(\theta, \varphi)$ , where  $B$  is the intrinsic brightness of a surface element  $dA$  at co-latitude  $\theta$  and longitude  $\varphi$ . We will define this set of spherical coordinates to be aligned such that the pole ( $\theta = 0$  or  $\pi$ ) matches the stellar spin axis. In this frame, we will define the observers line of sight as  $(\theta_0, \varphi_0)$ . We can now define  $\gamma$  as the angle between the outward normal of a point on the sphere and the observer's line of sight. Hence we can define the geometric foreshortening as (see A2):

$$\cos \gamma = \cos \theta \cos \theta_0 + \sin \theta \sin \theta_0 \cos(\varphi - \varphi_0) \quad (\text{A18})$$

Russell (1906) then defines the light curve as:

$$L = \frac{1}{R^2} \int_S B \cos \gamma \, dA \quad (\text{A19})$$

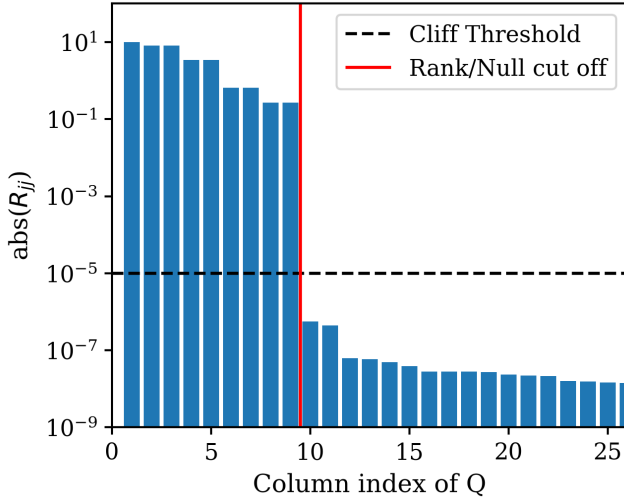


**Figure A1.** This figure shows the typical structure of  $\text{diag}(R)$ , with the cliff present demonstrating the cut off between the rank and null column. The numerical noise can be cleanly separated from the signals of interest.

here  $R$  is the distance of the element from the observer. For any star,  $R$  is essentially constant, so we will drop it. Here  $dA = \sin \theta d\theta d\varphi$  is the standard surface area element / Jacobian. [Russell \(1906\)](#) then expands:

$$B(\theta, \varphi) = Y_0 + Y_1(\theta, \varphi) + \dots + Y_n(\theta, \varphi) + \dots \quad (\text{A20})$$

He then goes on to state that the surface of stars satisfy all the necessary conditions to ensure the validity of this spherical harmonic expansion. In addition to  $\gamma$ , we can also define a new angle,  $\lambda$ , as the position angle on the apparent disk (i.e. the azimuth of the point around the line of sight). We can now describe any point on the surface of the star with the pair of co-ordinates  $(\theta, \varphi)$ , this is just spherical harmonics that are defined around a different pole. In the spherical harmonic basis, a rotation of the surface can simply be expressed as a linear combination of modes  $m$  within a degree  $\ell$ . That is to say we can express:

$$Y_\ell(\theta, \varphi) = a_{\ell,0} P_\ell(\cos \gamma) + \sum_{m=1}^{m=\ell} (a_{\ell,m} \cos m\lambda + b_{\ell,m} \sin m\lambda) P_\ell^m(\cos \gamma) \quad (\text{A21})$$

Here,  $P_\ell$  is a Legendre polynomial, and  $P_\ell^m$  are associated Legendre polynomials (see Appendix A1). He then explains that if  $\gamma = 0$ , then  $(\theta, \varphi) = (\theta_0, \varphi_0)$ ,  $P_\ell(\cos \gamma) = 1$ , and  $P_\ell^m(\cos \gamma) = 0$ . Hence:

$$a_0 = Y_\ell(\theta_0, \varphi_0) \quad (\text{A22})$$

He then considers the light curve as observed from the observers line of sight. If one then considers a stellar surface of just a single spherical harmonic, one gets:

$$L(\theta_0, \varphi_0) = \int_0^{2\pi} d\lambda \int_0^{\pi/2} \left[ Y_\ell(\theta_0, \varphi_0) P_\ell(\cos \gamma) + \sum_{m=1}^{\ell} (a_m \cos(m\lambda) + b_m \sin(m\lambda)) P_\ell^m(\cos \gamma) \right] \cos \gamma \sin \gamma d\gamma \quad (\text{A23})$$

Here the integration limits represent the visible hemisphere. Now, by integrating with respect to  $\lambda$ , all terms but the first vanish:

$$L(\theta_0, \varphi_0) = Y_\ell(\theta_0, \varphi_0) \int_0^{\pi/2} P_\ell(\cos \gamma) \cos \gamma \sin \gamma d\gamma \quad (\text{A24})$$

We can then substitute  $x = \cos \gamma$  (then  $dx = -\sin \gamma d\gamma$ ):

$$\int_0^1 x P_\ell(x) dx \quad (\text{A25})$$

[Russell \(1906\)](#) states that this is a well-known integral. For completeness, we will solve it below. Using Bonnet's recursive relationship for the Legendre polynomials:

$$(2\ell + 1)x P_\ell(x) = \ell P_{\ell-1}(x) + (\ell + 1)P_{\ell+1}(x) \quad (\text{A26})$$

Now integrate both sides w.r.t  $dx$  and define  $I_\ell := \int x P_\ell(x) dx$ , and  $A_\ell := \int P_\ell(x) dx$ , we get:

$$(2\ell + 1)I_\ell = \ell A_{\ell-1} + (\ell + 1)A_{\ell+1} \quad (\text{A27})$$

Another way of stating Bonnets recursive relation is:

$$(2\ell + 1)P_\ell(x) = \frac{d}{dx}(P_{\ell+1}(x) - P_{\ell-1}(x)) \quad (\text{A28})$$

If we integrate this between 0 and 1, we get:

$$(2\ell + 1)A_\ell = P_{\ell+1}(x) - P_{\ell-1}(x) \Big|_0^1 \quad (\text{A29})$$

given that  $P_\ell(1) = 1 \quad \forall \ell$ , we get:

$$A_\ell = \frac{P_{\ell+1}(0) - P_{\ell-1}(0)}{2\ell + 1} \quad (\text{A30})$$

A known property of Legendre polynomials is that they satisfy  $P_k(-x) = (-1)^k P_k(x)$ . That is to say, if  $k$  is odd, then  $P_k(0) = 0$ . Now, if we substitute this Equation (A30) into Equation (A27), we get:

$$(2\ell + 1)I_\ell = \frac{\ell}{2\ell + 1} [P_\ell(0) - P_{\ell-2}(0)] + \frac{\ell + 1}{2\ell + 1} [P_{\ell+2}(0) - P_\ell(0)] \quad (\text{A31})$$

As  $\ell$  is odd, then  $\ell + 2, \ell - 2$  must also be odd. Hence, for off  $\ell \geq 3$ , Equation (A25) and Equation (A24) both evaluate to zero, and are therefore invisible to photometry.

## REFERENCES

Agol E., Luger R., Foreman-Mackey D., 2020, *The Astronomical Journal*, 159, 123  
 Basri G., 2018, *The Astrophysical Journal*, 865, 142  
 Baumann I., Solanki S. K., 2005, *Astronomy & Astrophysics*, 443, 1061–1066  
 Bendek E. A., Noyes M., Flores C., Belikov R., Sirbu D., Mejia Prada C., Tuthill P., Guyon O., 2021, in Lystrup M., Batalha N., Tong E. C., Siegler N., Perrin M. D., eds, *Space Telescopes and Instrumentation 2020: Optical, Infrared, and Millimeter Wave*. SPIE, p. 171, doi:10.1117/12.2562994, <http://dx.doi.org/10.1117/12.2562994>  
 Berdyugina S. V., 2005, *Living Reviews in Solar Physics*, 2  
 Betancourt M., 2018, Calibrating Model-Based Inferences and Decisions, doi:10.48550/ARXIV.1803.08393, <https://arxiv.org/abs/1803.08393>  
 Brown A. G. A., 2025, Gaia: Ten Years of Surveying the Milky Way and Beyond, doi:10.48550/ARXIV.2503.01533, <https://arxiv.org/abs/2503.01533>  
 Carllitz L., 1961, *Archiv der Mathematik*, 12, 334–340  
 Carroll T. A., Kopf M., Strassmeier K. G., Ilyin I., 2008, *Proceedings of the International Astronomical Union*, 4, 633–644  
 Chiavassa A., Freytag B., Masseron T., Plez B., 2011, *Astronomy & Astrophysics*, 535, A22  
 Ciftja O., 2022, *Results in Physics*, 40, 105838  
 Croll B., et al., 2006, *The Astrophysical Journal*, 648, 607–613

Davenport J. R. A., Hebb L., Hawley S. L., 2015, *The Astrophysical Journal*, 806, 212

DeWarp L. E., Datin K. M., Guinan E. F., 2010, *The Astrophysical Journal*, 722, 343–357

Dholakia S., Pope B. J. S., 2025, Analytic Interferometry of Rotating Stellar Surfaces, [doi:10.48550/ARXIV.2509.25433](https://doi.org/10.48550/ARXIV.2509.25433), <https://arxiv.org/abs/2509.25433>

Eriksson U., Lindegren L., 2007, *Astronomy & Astrophysics*, 476, 1389–1400

Evans N. R., et al., 2024, *The Astrophysical Journal*, 971, 190

Fisher R. A., 1935, *Journal of the Royal Statistical Society*, 98, 39

Gardner T., et al., 2022, *The Astronomical Journal*, 164, 184

González A., 2009, *Mathematical Geosciences*, 42, 49–64

Gully-Santiago M. A., et al., 2017, *The Astrophysical Journal*, 836, 200

Harmon R. O., Crews L. J., 2000, *The Astronomical Journal*, 120, 3274–3294

Hathaway D. H., Choudhary D. P., 2008, *Solar Physics*, 250, 269–278

Hauboix X., et al., 2009, *Astronomy & Astrophysics*, 508, 923–932

Huber D., Zwintz K., team t. B., 2020, Solar-Like Oscillations: Lessons Learned & First Results from TESS, [doi:10.48550/ARXIV.2007.02170](https://doi.org/10.48550/ARXIV.2007.02170), <https://arxiv.org/abs/2007.02170>

Ji J.-H., et al., 2022, *Research in Astronomy and Astrophysics*, 22, 072003

Khalid Z., Kennedy R. A., McEwen J. D., 2016, *Applied and Computational Harmonic Analysis*, 40, 470–504

Klein B., et al., 2025, *Monthly Notices of the Royal Astronomical Society*, 542, 2714–2732

Kochukhov O., 2016, Doppler and Zeeman Doppler Imaging of Stars. Springer International Publishing, p. 177–204, [doi:10.1007/978-3-319-24151-7\\_9](https://doi.org/10.1007/978-3-319-24151-7_9), [http://dx.doi.org/10.1007/978-3-319-24151-7\\_9](http://dx.doi.org/10.1007/978-3-319-24151-7_9)

Kowalski A. F., 2024, *Living Reviews in Solar Physics*, 21

Kővári Z., et al., 2021, *Astronomy & Astrophysics*, 650, A158

Ludwig H.-G., 2005, *Astronomy & Astrophysics*, 445, 661–671

Luger R., Agol E., Foreman-Mackey D., Fleming D. P., Lustig-Yaeger J., Deitrick R., 2019, *The Astronomical Journal*, 157, 64

Luger R., Foreman-Mackey D., Hedges C., Hogg D. W., 2021, *The Astronomical Journal*, 162, 123

Makarov V. V., Beichman C. A., Catanzarite J. H., Fischer D. A., Lebreton J., Malbet F., Shao M., 2009, *The Astrophysical Journal*, 707, L73–L76

Michel V., Simons F. J., 2017, *Inverse Problems*, 33, 125016

Montet B. T., Tovar G., Foreman-Mackey D., 2017, *The Astrophysical Journal*, 851, 116

Morris B. M., Hebb L., Davenport J. R. A., Rohn G., Hawley S. L., 2017, *The Astrophysical Journal*, 846, 99

Morris B. M., Agol E., Davenport J. R. A., Hawley S. L., 2018a, *Monthly Notices of the Royal Astronomical Society*, 476, 5408–5416

Morris B. M., Agol E., Davenport J. R. A., Hawley S. L., 2018b, *The Astrophysical Journal*, 857, 39

Mulder J. J. C., 2000, *Journal of Chemical Education*, 77, 244

Muraközy J., 2021, *The Astrophysical Journal*, 908, 133

Musin O. R., Tarasov A. S., 2014, The Tamnes problem for  $N=14$ , [doi:10.48550/ARXIV.1410.2536](https://doi.org/10.48550/ARXIV.1410.2536), <https://arxiv.org/abs/1410.2536>

Namekata K., et al., 2019, *The Astrophysical Journal*, 871, 187

Nemati B., et al., 2020, in Lystrup M., Batalha N., Tong E. C., Siegler N., Perrin M. D., eds, Space Telescopes and Instrumentation 2020: Optical, Infrared, and Millimeter Wave. SPIE, p. 268, [doi:10.1117/12.2574986](https://doi.org/10.1117/12.2574986), <http://dx.doi.org/10.1117/12.2574986>

PVC (Research Infrastructure), UNSW Sydney 2010, Katana, [doi:10.26190/669X-A286](https://doi.org/10.26190/669X-A286), <https://researchdata.edu.au/katana/1733007>

Paladini C., et al., 2017, *Nature*, 553, 310–312

Price M. A., Pratley L., McEwen J. D., 2021, Sparse image reconstruction on the sphere: a general approach with uncertainty quantification, [doi:10.48550/ARXIV.2105.04935](https://doi.org/10.48550/ARXIV.2105.04935), <https://arxiv.org/abs/2105.04935>

Price M. A., Polanska A., Whitney J., McEwen J. D., 2024, Differentiable and accelerated wavelet transforms on the sphere and ball, [doi:10.48550/ARXIV.2402.01282](https://doi.org/10.48550/ARXIV.2402.01282), <https://arxiv.org/abs/2402.01282>

Rackham B. V., et al., 2023, *RAS Techniques and Instruments*, 2, 148–206

Reinhold T., Reiners A., Basri G., 2013, *Astronomy & Astrophysics*, 560, A4

Rice J., 2002, *Astronomische Nachrichten*, 323, 220–235

Rice J. B., Strassmeier K. G., 1998, *A&A*, 336, 972

Roddy P. J., McEwen J. D., 2022, *IEEE Transactions on Signal Processing*, 70, 6142–6153

Roettenbacher R. M., et al., 2016, *Nature*, 533, 217–220

Roettenbacher R. M., et al., 2017, *The Astrophysical Journal*, 849, 120

Russell H. N., 1906, *The Astrophysical Journal*, 24, 1

Shapiro A. I., Solanki S. K., Krivova N. A., 2021, *The Astrophysical Journal*, 908, 223

Strassmeier K. G., 1999, *A&A*, 347, 225

The Theia Collaboration et al., 2017, Theia: Faint objects in motion or the new astrometry frontier, [doi:10.48550/ARXIV.1707.01348](https://doi.org/10.48550/ARXIV.1707.01348), <https://arxiv.org/abs/1707.01348>

Tuthill P. G., et al., 2018, in Optical and Infrared Interferometry and Imaging VI. SPIE, p. 990403, [doi:10.1117/12.2313269](https://doi.org/10.1117/12.2313269)

Utsunomiya S., Yasuda S., Yano T., Niwa Y., Kobayashi Y., Kashima S., Goda N., Yamada Y., 2014, in Space Telescopes and Instrumentation 2014: Optical, Infrared, and Millimeter Wave. SPIE, p. 91430Z, [doi:10.1117/12.2055929](https://doi.org/10.1117/12.2055929)

Vallenari A., et al., 2023, *Astronomy & Astrophysics*, 674, A1

Vashishth V., Karak B. B., 2024, The role of meridional flow in the generation of solar/stellar magnetic fields and cycles, [doi:10.48550/ARXIV.2407.16620](https://doi.org/10.48550/ARXIV.2407.16620), <https://arxiv.org/abs/2407.16620>

Walkowicz L. M., Basri G., Valenti J. A., 2013, *The Astrophysical Journal Supplement Series*, 205, 17

Zic A., et al., 2020, *The Astrophysical Journal*, 905, 23

This paper has been typeset from a *T<sub>E</sub>X/L<sub>A</sub>T<sub>E</sub>X* file prepared by the author.